Desalination and Water Treatment
www.deswater.com

doi: 10.5004/dwt.2020.25129

181 (2020) 300–320
March

Graphene-supported iron-based composites: a review of applications to wastewater treatment

Xianliang Wu[a], Rensheng Cao[a], Jiwei Hu[a,b,*], Chao Zhou[a], Liya Fu[c], Xionghui Wei[d]

[a]*Guizhou Provincial Key Laboratory for Information Systems of Mountainous Areas and Protection of Ecological Environment, Guizhou Normal University, Guiyang 550001, Guizhou, China, Tel. +86-851-86702710; emails: jiweihu@yahoo.com/jwhu@gznu.edu.cn (J. Hu), wuxianliang1995@163.com (X. Wu), 18230825324@163.com (R. Cao), felixchou613@yahoo.com.cn (C. Zhou)*
[b]*Cultivation Base of Guizhou National Key Laboratory of Mountainous Karst Eco-environment, Guizhou Normal University, Guiyang 550001, Guizhou, China*
[c]*Research Center of Water Pollution Control Technology, Chinese Research Academy of Environmental Sciences, Chaoyang District, Beijing 100012, China, email: fuliya1986@126.com*
[d]*Department of Applied Chemistry, College of Chemistry and Molecular Engineering, Peking University, Beijing 100871, China, email: xhwei@pku.edu.cn*

Received 29 March 2019; Accepted 6 November 2019

ABSTRACT

Water environment has been deteriorating in the recent decades due to the rapid industrialization, population expansion and urbanization. Large volumes of wastewater contaminated with heavy metals and organic pollutants are discharged into the environment not only causing a serious danger to the human life but also threatening the eco-environment. It is thus of pivotal importance to remove these pollutants from wastewater. Graphene has been adopted for various applications due to a variety of excellent properties, such as large specific surface area, good solution-dispersibility and high mechanical strength. The large quantities of oxygen-containing functional groups of graphene can strengthen its adsorption capacity for contaminants. Iron-based materials exhibit special physical and chemical properties, which have been successfully adopted to a broad range of applications, including catalysis, biosensors, and removal of environmental pollutants. Graphene-supported iron-based composites have good magnetic properties so that they can be readily separated from water after the adsorption process. It is particularly important to study the pollutants removal processes; thus different kinetics and isotherm models were used to investigate these processes. This review is focused on the methodology for the synthesis and characterization of graphene-supported iron-based composites, and their applications in wastewater treatment.

Keywords: Graphene-supported iron-based composites; Pollutants; Equilibrium isotherms, Removal kinetics; Thermodynamics; Artificial intelligence

1. Introduction

The scarcity of water resources has become a serious concern with the rapid population growth, industrialization, agricultural activities and environmental changes [1]. Large volumes of sewage and wastewater are generated from households and various industries [2], such as mining, dyes, plastics [3], textile [4], paper, food [5], coating [6], rubber, fertilizer, lighting, pesticides, cosmetics, pharmaceuticals [7], electronics, electroplating, wood, and leather [8]. The wastewater contaminated with heavy metals and organic pollutants is discharged into the natural water not only causing a serious danger to the human life but also threatening the eco-environment [9,10]. There are various methods

* Corresponding author.

that have been developed to remove these pollutants from aqueous solutions, such as oxidation, precipitation, reverse osmosis, ion exchange [11,12], membrane filtration [13,14], solvent extraction [15], flocculation [16], coagulation [17], electrocoagulation/electroflocculation [18–20], electrochemical reduction/precipitation [21–24], evaporation, adsorption, and biosorption [25–27].

To effectively remove pollution from wastewater, various iron-based materials (i.e., Fe^0, Fe_3O_4, Fe_2O_3, FeOOH, $MnFe_2O_4$, $CuFe_2O_4$, and $ZnFe_2O_4$) were proven as effective adsorbents in the removal processes. Nanoscale zero-valent iron (NZVI) particles have been considered as one of the most promising permeable barrier materials applied in wastewater treatment because of their extremely small particle size, large specific surface area, and high injectability [28,29]. Especially as an active metal, it has an excellent in-situ reactivity (reducibility) with a standard redox potential of E^0 (Fe^{2+}/Fe^0) = –0.44 V. Thus, NZVI can reduce the oxidizing ions or some compounds in wastewater. Fe_2O_3 is an abundant, cost-effective and environmentally benign n-type semiconductor with the band-gap of 2.2 eV. It has been extensively studied due to its fascinating and peculiar physicochemical properties and wide potential applications in different fields, for example, water splitting and catalysis [30,31]. Ferroferric oxide (Fe_3O_4) nanoparticles (NPs) are relatively inexpensive and earth-abundant elements that are used for a variety of technologies for catalysts, magnetic materials, electrode materials, and environmental and biomedical fields [32]. Fe_3O_4 magnetic nanoparticles that were reported to have a peroxidase-like activity could activate H_2O_2, leading to the oxidative degradation of phenol and other organic pollutants [33,34]. Fe_3O_4 quantum dots are the most prominent class of magnetic NPs. These quantum dots have been widely utilized in biological and environmental applications [35], because they have unique magnetic properties, biocompatibility and allow the rapid separation of target molecules from the samples simply by applying an appropriate magnetic field [35,36]. Ferric oxyhydroxide (FeOOH) exhibits a tunnel-type structure where iron atoms are strongly bonded to the framework that constitutes the tunnels, eliminating the possibility of structural collapse [37]. It has been extensively applied for electrode materials, organic pollutants degradation, water purification, and human sensing applications because of its merits such as corrosion resistance, environmental friendliness and low cost [38]. FeOOH, as a good precursor for the fabrication of α-Fe_2O_3, γ-Fe_2O_3, and Fe_3O_4, has primarily three crystalline patterns: α-, β-, and γ-FeOOH [39]. MFe_2O_4 (where M = Mn, Cu, Ni, and Co) has shown a great potential for applications owing to their unique optical, magnetic, and electrical properties [40]. Zinc ferrite ($ZnFe_2O_4$) is a soft magnetic semiconductor with excellent photoelectric conversion properties [41], which have the advantages of good stability, high magnetic properties, and suitability [42,43]. However, these iron-based particles are actually prone to aggregate by spontaneous magnetization that decreases specific surface area [44]. Incorporation of nanoparticles into carbon or polymer matrix can prevent the aggregation and their susceptible oxidation [45].

The ability to prepare graphene and its derivatives has triggered intense research in two-dimensional nanomaterials since the high quality, few-atom-thick nanosheets (including single-layer) were isolated from graphite [46]. Graphene is an atomic sheet of sp^2-bonded carbon atoms that are arranged into a honeycomb structure [47,48]. In the recent years, a rapid progress has been made in fabricating transistor-like devices from graphene and measuring its transport properties [49]. The local charge disorder, substrate-induced structural distortion, edge structure, and even atomic scale defects could be highly important for the transport properties of graphene [50–53]. The mono-layered graphene has a large specific surface area [54], good solution-dispersibility, excellent electronic conductivity [55], exceptional mechanical properties [56], unique thermal and optical properties [57–59]; therefore it has been adopted in various applications such as nanoelectronics, batteries, flexible displays, touch screens, solar cells, composite materials [60], supercapacitors, actuators, sensors, reinforcing materials, catalysts, adsorbents, and hydrogels [31,61,62]. In addition, the chemical structure of graphene oxide (GO) is decorated with various oxygenated functionalities [63,64], for example, hydroxyl, epoxy on the basal plane and carbonyl, carboxylic acid at the edges [65,66]. These hydrophilic oxygen functionalities make GO extensively dispersible in water as well as some organic solvents, and easier to intercalate solvents [67]. The large quantities of oxygen-containing functional groups can also strengthen their adsorption capacity toward contaminants [68–70], hence GO is a good candidate for supporting metal oxide nanoparticles and the immobilization of a large number of enzymes [47,71,72]. Graphene is difficult to separate from solution phase after an adsorption process via traditional filtration and centrifugation. Graphene-supported iron-based composites have good magnetic properties, which provide a solution to this problem because the magnetic cores ensure the convenient magnetic separation after the adsorption process [59,73]. Recently, a considerable attention has been focused on the application of magnetic separation technology to solve environmental problems. A series of techniques based on the use of magnetic or magnetizable adsorbents, carriers and cells, have been employed in microbiology, biochemistry, mining ores, cell biology, and environmental technologies (e.g., use of polymer-coated magnetic particles for oil spill remediation, magnetite particles to accelerate the coagulation of sewage and magnetic iron-based composites for the adsorption of pollutants) [59].

In this review, we focus on the synthesis and characterization methodologies of graphene-supported iron-based composites, and adsorption isotherms, kinetics, thermodynamic studies as well as artificial intelligence (AI) based process optimization approaches for pollutants removal using these composites. We also summarize the regeneration and reusability of these composites in wastewater treatment. The applications mainly include the following two aspects: (a) heavy metals removal and (b) organic pollutants removal.

2. Preparation and characterization of graphene-supported iron-based composites

2.1. Preparation of graphene-supported iron-based composites

The synthesis of graphene has attracted much attention, and the main methods of preparing graphene are as follows:

exfoliation and cleavage, electrochemical preparation, thermal chemical vapor deposition techniques, plasma enhanced chemical vapor deposition techniques, wet ball milling, micromechanical exfoliation, epitaxial growth, the reduction of graphene oxide (GO) solution, organic synthesis, and Hummers' method [74].

Exfoliation and cleavage methodology uses mechanical or chemical energy to break these weak bonds and separate out individual graphene sheets. The first attempt in this direction was made by Viculis et al. [75], who used potassium metal to intercalate a pure graphite sheet and then exfoliate it with ethanol to form dispersion of carbon sheets [76,77]. Graphene was synthesized by thermal chemical vapor deposition [76,78]. In this work, camphor was used to synthesize graphene on Ni foils [78]. Obraztsov et al. [79] proposed a direct current discharge plasma enhanced chemical vapor deposition method to produce the nanostructured graphite-like carbon. This process used Si wafer and Ni, W, Mo, and some other metal sheets as substrates and a gas mixture of CH_4 and H_2, with a total gas pressure of 10 to 150 Torr. Wet ball milling was used to exfoliate graphite platelets into graphene in a liquid medium. Multi-layered graphite nanosheets with a thickness of 30 to 80 nm were dispersed into N,N-dimethylformamide and exfoliated by shear-force-dominated ball milling carried out in a planetary mill. After high-speed centrifugation, irregular shaped single- and few-layer graphene sheets (≤3 layers) having a thickness around 0.8–1.8 nm were obtained from the supernatant [80].

Hummers' method is commonly used for the synthesis of graphene. Briefly, the mixture of graphite and $NaNO_3$ was added into a beaker with a certain amount of 98 wt.% H_2SO_4 at 15°C and a suspension was obtained. Then $KMnO_4$ powder acting as an oxidation agent was gradually added into the suspension with continuous stirring. After reaction at different temperatures, a certain amount of deionized water was added into the mixture slowly, then a large amount of heat was released when conc. H_2SO_4 was diluted. After 15 min of reaction, a certain amount of hot water and 30% H_2O_2 solution were added into the mixture, respectively, with continuously stirring. The bright yellow suspension resulted was filtered by the qualitative filter paper when it was still hot, and the solid mixture was washed with dilute HCl solution and distilled water and dried in vacuum oven at 70°C for 24 h.

The synthesis of graphene-supported iron-based composites generally has involved the following methods: co-precipitation [81], chemical co-precipitation [59], ultrasonic-assisted reverse co-precipitation [34], phytochemistry [82], polyol process and impregnation [83], layer-by-layer assembly [44], three-step method [21], urea-assisted auto combustion synthesis followed by an annealing step [84], chemical precipitation [85], impregnation [86], solvothermal process [87], ultrasound-assisted in situ precipitation [71], aqueous-phase [88], facile one-step reaction route [89], facile one-step hydrothermal process [90], facile two-step [91,92], citrate precursor [42], sol-gel [42] and self-assembly [8,93]. Figs. 1 and 2 show the synthesis process.

Sonication is an important factor affecting the preparation of graphene oxide (Table 1). Especially, the different ultrasonic powers can significantly influence the efficiency of peeling graphite oxide to graphene oxide and the transverse dimension of graphite oxide. The higher the ultrasonic power and the longer the ultrasonic time, the higher the peeling efficiency is. With the prolongation of ultrasonic treatment time, the particle size of graphite oxide decreases gradually due to the continual exfoliation of the lamellar structure of graphite oxide sheets and the thinning of the lamellar structure;

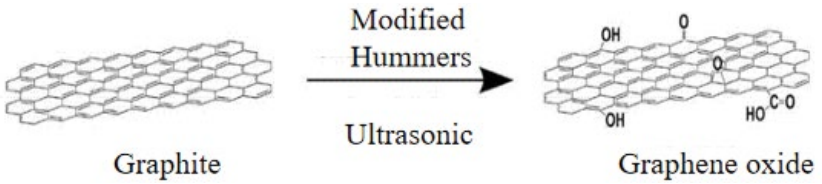

Fig. 1. Preparation of graphene oxide.

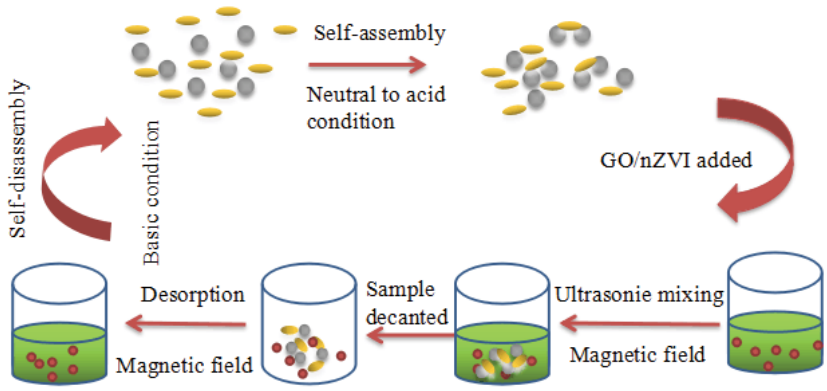

Fig. 2. Preparation of graphene-supported iron-based materials.

Table 1
Sonochemical methods for the preparation of nanocomposites

Materials	Sonochemical methods	Description	References
SnO_2–graphene nanocomposite	Prepared 25 mL GO solution was diluted with 450 mL deionized water followed by the addition of 8.5 mL of aqueous HCl solution (35 wt.%) under ultrasonic irradiation (5 min). Then 3 g $SnCl_2{\cdot}2H_2O$ was added into resulted GO-HCl aqueous solution and was again ultrasonicated for 30 min at room temperature	This study reports ultrasound assisted preparation of SnO_2–graphene nanocomposite in three steps. In the first step, the preparation of graphene oxide using modified Hummers' method was accomplished in the presence of ultrasonic irradiation. In the second step, preparation of graphene oxide by ultrasonication has been reported. Finally, ultrasound assisted fabrication of SnO_2–graphene nanocomposite was carried out by the solution based synthesis route in the presence of GO	[94]
Fe_3O_4-Graphene Nanocomposites	Solution of GO was prepared by adding 40 mg GO to 40 mL of DI water. 110 mg $FeCl_3$ and 43 mg $FeCl_2$ was added to 50 mL DI water, well mixed with a prepared GO solution and then the temperature of the mixture was increased to 85°C. The pH of the resulting solution was maintained at 10 by adding 30 wt.% ammonia solution and resulting solution was ultrasonicated for 30 min	Synthesis of graphene-Fe_3O_4 nanocomposites was carried out by ultrasound assisted coprecipitation of iron (II) and (III) chlorides in the presence of GO	[95]
A stable graphene dispersion with high concentration	A 0.14 g portion of hydrazine (50%) was added to the dispersion at a temperature of 65°C, a graphene dispersion was collected by filtration with a 200 mesh net at different reaction times, such as 10, 20, 40, 60, 70, and 120 min.	By replacing mechanical stirring with ultrasonic irradiation, the aggregation of various intermediates is effectively suppressed during the process of GO reduction	[96]
Graphene-Ce-TiO_2 photocatalyst nanocomposite	Initially 5 mL of titanium isopropoxide was added to 4 mL of NaOH solution (1 N). 3 mL of as prepared solution of titanium isopropoxide and NaOH was added to 10 mL of GO solution (900 mg GO was dispersed in 250 mL water). The whole prepared mixture was sonicated for 1 h and this leads to the formation of graphene-TiO_2 photocatalyst nanocomposites	Ultrasound-assisted synthesis of graphene-TiO_2, Graphene Ce-TiO_2 and Graphene-Fe-TiO_2 ternary hybrid photocatalyst nanocomposite was carried out	[92]
Graphene-Fe-TiO_2 ternary hybrid	Initially, 1 g of GO and 5 mL titanium isopropoxide was added to 50 mL 2-propanol and was sonicated for 30 min. Two separate solutions were prepared by the addition of 0.06 g ferric nitrate in 20 mL distilled water and 2.7 g NaOH in 50 mL distilled water. The prepared NaOH (5 mL in every 30 s) and ferric nitrate (2 mL in every 30 s) solutions were added continuously to as prepared GO and titanium isopropoxide solution in 2-propanol in the presence of ultrasonic irradiations in order to control the reaction and in turn to control the particle size for uniform dispersion of dopant and TiO_2 on graphene nanosheets. This mixture was sonicated for 30 min after complete addition of NaOH and ferric nitrate solutions	Prepared photocatalyst was studied for the degradation of crystal violet dye and the photocatalytic activity was compared with that of graphene-TiO_2 photocatalyst	
Rhodium–graphene nanocomposite	15 mL of GO solution (0.5 mg mL^{-1}) was mixed with 10 mL of 1×10^{-3} M solution of $RhCl_3{\cdot}xH_2O$, and the whole mixture was sonicated for 20 min in a bath sonicator	Rhodium nanoparticles–graphene nanocomposites were prepared by a simple borohydride reduction of $RhCl_3{\cdot}xH_2O$ on very stable GO sheets	[97]

thus the particle size decreases significantly with the prolongation of ultrasonic treatment time. At the same time, some graphite oxide fragments were produced in the ultrasonic process, which may be caused by the interrupted ultrasonic dispersion. The high temperature and high pressure environment produced by ultrasonic cavitation provides the energy needed for the formation of micro-particles, which makes the formation rate of precipitated nuclei increase by several orders of magnitude. The increase of the formation rate of precipitated nuclei reduces the particle size of precipitated particles, and the high temperature generated by ultrasonic cavitation and the large number of bubbles on the surface of solid particles greatly reduce the specific surface Gibbs free energy of the nuclei. It can inhibit the aggregation and growth of nuclei. In addition, the shock wave produced by ultrasonic cavitation and the smashing of micro-jet make the precipitation exist as uniform micro-particles. Thus, the powder prepared by this method has a smaller particle size with more uniform distribution.

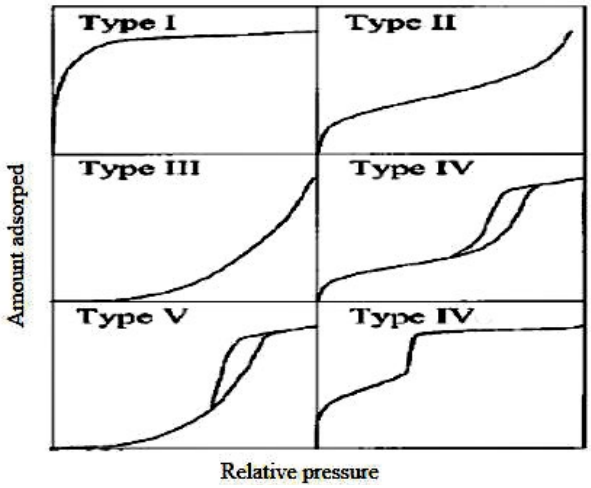

Fig. 3. N_2 adsorption–desorption isotherms.

2.2. Preparation of ordered mesoporous materials

A mesoporous material is a material containing pores with diameters between 2 and 50 nm in accordance with the IUPAC nomenclature. For comparison, IUPAC defines microporous material as a material having pores smaller than 2 nm in diameter and macroporous material as a material having pores larger than 50 nm in diameter. This classification is rooted in a gas adsorption behavior of the pores: micropores are sufficiently small to adsorb gases at low pressures through the micropore filling, mesopores exhibit monolayer–multilayer adsorption of molecules followed by the complete filling of pores via capillary condensation, and macropores demonstrate virtually unrestricted monolayer–multilayer adsorption. According to IUPAC, a mesoporous material can be disordered or ordered in a mesostructure. In crystalline inorganic materials, mesoporous structure noticeably limits the number of lattice units, and this significantly changes the solid-state chemistry. For example, the battery performance of mesoporous electroactive materials is significantly different from that of bulk structure. The classification of N_2 adsorption–desorption isotherms is as follows (Fig. 3):

In 1992, a groundbreaking method for the synthesis of high-surface-area mesoporous materials was reported, in which surfactant micelles serve as templates for periodically arranged mesopores of uniform size and well-defined shape. Under the basic conditions, alkyltrimethylammonium surfactants were shown to assemble with silicates to form ordered arrays of surfactant micelles embedded in the silicate framework. These products were named as the M41S family of materials. The ultrasonic time and power can significantly affect the particle size and pore ordering of prepared materials. Ultrasound can help obtain materials with higher order than hydrothermal method in the same reaction time. Generally, ultrasonic stirring is more advantageous than ordinary stirring to maintain the stability in the prepared process of mesoporous materials [98]. Highly ordered mesoporous materials have attracted an increasing attention for catalyst support materials because of their high surface area, narrow pore size distribution, uniform porous connections and adjustable pore symmetry. The wide and ordered pore channels are especially useful for the separation of large biomolecules or natural products and, meanwhile, provide a broad space for fast mass transfer, which is highly beneficial in high-rate supercapacitors and heterogeneous catalysis.

2.3. Characterization techniques of graphene-supported iron-based composites

In order to develop highly efficient and low-cost materials for removing environmental pollutants, the structure and composition of different graphene-supported iron-based composites must be clarified; therefore they were characterized by a variety of techniques: powder X-ray diffraction (XRD), vibrational sample magnetometer [82], attenuated total reflectance-infrared, thermogravimetric analysis [62], scanning electron microscopy (SEM), field emission scanning electron microscopic (FE-SEM) [92], transmission electron microscopy (TEM), Fourier transform infrared spectroscopy (FTIR), N_2 adsorption, zeta potential, Raman spectroscopy, X-ray photoelectron spectroscopy (XPS) [99], X-ray absorption near edge spectroscopy (XANES) [45], total organic carbon, photoluminescence (PL) [41], energy-dispersive X-ray spectroscopy (EDS) [100], Brunauer–Emmett–Teller and energy dispersive X-ray spectrometry [101] and synchrotron radiation techniques [102]. Among them, Raman spectroscopy is used to characterize materials, measure temperature, and find the crystallographic orientation of a sample. As with single molecules, a solid material can be identified by characteristic phonon modes. Information on the population of a phonon mode is given by the ratio of the Stokes and anti-Stokes intensity of the spontaneous Raman signal. XPS spectra are obtained by irradiating a material with a beam of X-rays while simultaneously measuring the kinetic energy and number of electrons that escape from the top 0 to 10 nm of the material being analyzed. It is used to analyze inorganic compounds, metal alloys, semiconductors, polymers, elements, catalysts, glasses, ceramics, paints, papers, inks, woods, plant parts, make-up, teeth, bones, medical implants,

bio-materials, viscous oils, glues, ion-modified materials and many others. It is especially useful for ceramics, polymers, powders, metals, metal inclusions, epoxy resins, and semiconductor because of higher magnification, large field of vision, stereoscopic image and simple sample preparation. The parameters obtained from the characterization include crystal structure, magnetism, shape, granularity, size distribution, chemistry, valence state, agglomeration/dispersion, and specific surface area. These properties can affect the environmental remediation ability of graphene-supported iron-based composites [93].

New characterization techniques are continuously emerging in the nano field. Some mainstream and cutting-edge characterization techniques are summarized below in more details.

2.3.1. Atomic probe tomography

Researchers have tried to reconstruct the three-dimensional view of matter at nanoscale, and then explain the macroscopic properties of materials and consciously adjust or improve the microstructures matching the properties [103]. Atomic probe tomography (APT) can determine the types of atoms and reconstruct their spatial positions intuitively, which can show the three-dimensional spatial distribution of atoms of different elements in materials relatively authentically. APT has become the most high spatial resolution analysis and testing method at present. Essentially, as atoms on the surface of the specimen field evaporate one at a time and fly toward a two-dimensional position-sensitive detector, their hit position in x and y is recorded. Gradually, each atom on the surface evaporates and exposes the underlying layer(s). The sequence of atom hits on the detector can be used to track both the serial evaporation of atoms in a given layer and the serial evaporation of the layers. Taylor et al. [104] reported that the distribution of Fe resulted from the autocatalytic interaction of aqueous Fe(II) with the hematite (α-Fe_2O_3) (001) surface was directly mapped in three dimensions (3D) for the first time, using the Fe isotopic labeling and APT. Tamion et al. [171] described that a careful investigation of the structure and chemistry of the multilayers was carried out using a 3D atom probe.

2.3.2. Secondary-ion mass spectrometry

Secondary-ion mass spectrometry (SIMS) is a technique used to analyze the composition of solid surfaces and thin films by sputtering the surface of the specimen with a focused primary ion beam and collecting and analyzing ejected secondary ions [105]. The mass/charge ratios of these secondary ions are measured with a mass spectrometer to determine the elemental, isotopic, or molecular composition of the surface to a depth of 1–2 nm. Due to the large variation in ionization probabilities among different materials, SIMS is generally considered to be a qualitative technique, although quantification is possible with the use of standards. SIMS is the most sensitive surface analysis technique, with elemental detection limits ranging from parts per million to parts per billion. Detection limits for most trace elements are between 1,012 and 1,016 atoms per cubic centimetre, depending on the type of instrumentation used, the primary ion beam used and the analytical area, and other factors. Samples as small as individual pollen grains and microfossils can yield results by this technique.

2.3.3. X-ray absorption near edge structure

X-ray absorption near edge structure (XANES), also known as near edge X-ray absorption fine structure (NEXAFS), is an absorption spectroscopy that indicates the features in the X-ray absorption spectra of condensed matter due to the photoabsorption cross section for electronic transitions from an atomic core level to final states in the energy region of 50–100 eV above the selected atomic core level ionization energy, where the wavelength of the photoelectron is larger than the interatomic distance between the absorbing atom and its first neighbor atoms. It can provide information about the electronic configuration, stereochemistry, and oxidation states of the metallic atoms [106]. In addition, extended X-ray absorption fine structure (EXAFS) spectroscopy can be used to investigate the atomic arrangement of heavy metals in farming soils in terms of their bond distance, number, and kind of near neighbors, besides thermal and static disorders [107].

2.3.4. Scanning electron microscopy and transmission electron microscopy

SEM is an electron microscope that produces images of a sample by scanning the surface with a focused beam of electrons. The electrons interact with atoms in the sample, producing various signals that contain information about the surface topography and composition of the sample [108,109]. It has widely been employed in nanomaterials, metallurgy, biology, medicine, semiconductor materials and devices, geological exploration, pest control, disaster (fire and failure analysis) identification, criminal reconnaissance, and gemstone identification. Especially, it is an important characterization technique for graphene-supported iron-based composites to obtain useful information for the surface morphology of the sample. Fan et al. [107] reported that the nZVI nanoparticles synthesized were aggregated in the bare form, while these nanoparticles were dispersed well on reduced graphene oxide. Ruan et al. [110] described that the average diameter of Fe/Ni particles was approximately 66 nm in the bare form and 42 nm on the rGO, respectively. The Fe/Ni nanoparticles are uniformly dispersed on the rGO surface, demonstrating the inhibition effect of rGO supporting on the Fe/Ni nanoparticles aggregation.

Spherical aberration corrected scanning transmission electron microscopy-energy dispersive X-ray spectroscopy (Cs-corrected STEM-EDS) does not only have sub-Egyptian spatial resolution, but a variety of experimental functions as well. Meanwhile, it is an effective method to study the structure–activity relationship of materials by studying the crystal structure and corresponding electronic structure characteristics of materials at the atomic scale, so as to understand the relationship between the micro-crystal structure and properties of samples. When electrons interact with matter, the initial X-ray can be excited by focusing incident electrons. The characteristic X-ray wavelength and energy emitted by different elements are different; therefore, it has

a very wide range of applications in the fields of physics, materials science, and chemistry. Similarly to Cs-corrected STEM, high-angle hollow-cone dark-field transmission electron microscopy (HADF-TEM) can also investigate the "core/shell" structure of nanocomposite particles, which is an imaging mode of specialized transmission electron microscopes that allows for direct imaging of the atomic structure of the sample. HADF-TEM is a powerful tool to study properties of materials on the atomic scale, such as semiconductors, metals, nanoparticles, and sp^2-bonded carbon (e.g., graphene, nanotubes). The contrast of light-dark field image (i.e., light-dark difference in different regions) of crystal thin film sample is formed by the difference of diffraction intensity caused by the structure or orientation of different parts of the sample. Therefore, it is called diffraction contrast, and the image formed mainly by the mechanism of diffraction contrast is called derivative contrast image. In HADF-TEM equipment, if the transmitted beam is allowed to image through the objective beam, it is called the bright field image, whereas it is called the dark field image if only a diffraction beam is allowed to image through the objective beam.

2.3.5. X-ray fluorescence and X-ray fluorescence imaging

X-ray fluorescence (XRF) is the characteristic emission of "secondary" (or fluorescent) X-rays from a material that has been excited by bombarding with high-energy X-rays. The phenomenon is widely used for elemental analysis and chemical analysis, particularly to investigate metals, glass, ceramics, and building materials in geochemistry, forensic science, archaeology, and arts (such as paintings and murals). XRF imaging uses a device to inundate the sample with X-ray waves. Based on the feedback received from atoms in the sample, it is able to calculate the material type. Because every element exhibits unique characteristics when irradiated, individual atoms can be detected allowing for a complete breakdown of chemical composition. For coating thickness measurements by x-ray fluorescence, a secondary equipment (such as diode) is normally used to ensure the accuracy.

2.3.6. X-ray diffraction

XRD analysis is based on constructive interference of monochromatic X-rays and a crystalline sample. The X-rays are generated by a cathode ray tube, filtered to produce monochromatic radiation, collimated to concentrate, and directed toward the sample. The interaction of the incident rays with the sample produces constructive interference (and a diffracted ray) when the conditions satisfy Bragg's Law ($n\lambda = 2d \sin \theta$). This law relates the wavelength of electromagnetic radiation to the diffraction angle and the lattice spacing in a crystalline sample. The characteristic XRD pattern generated in a typical XRD analysis provides a unique "fingerprint" of the crystals present in the sample. When properly interpreted, by comparison with standard reference patterns and measurements, this fingerprint allows identification of the crystalline form. If single crystals of sufficient size cannot be obtained, various other X-ray methods can be applied to obtain less detailed information, which include fiber diffraction, powder diffraction (if the sample is not crystallized), small-angle X-ray scattering (SAXS) and small-angle X-ray diffraction (SA-XRD).

2.3.7. Nitrogen adsorption

Nitrogen adsorption is an effective method to characterize porous materials. Orderliness of materials can also be partially reflected in the adsorption–desorption curve, but porous materials can be further characterized by the SAXS, SA-XRD and high-resolution transmission electron microscopy (HR-TEM). In the SA-XRD test, some false peaks are easy to appear due to the occlusion of the sample to X-ray, and the experimental operation requirements are high. SAXS uses a translucent light path to test the sample, avoiding the phenomenon of false peaks because the sample is not flattened or zero-point surface is not placed. If ordered mesoporous materials possess large ordered size, the ordered arrangement of channels can be easily seen by HR-TEM images, and the pore size of materials can be measured afterwards. Generally, SAXS and SA-XRD combined with HR-TEM is an effective method to characterize ordered porous materials, and full pore size analysis can be carried out by combining nitrogen adsorption and desorption.

3. Studies of pollutants removal processes

3.1. Pollutants removal with the aid of AI-based high precision process optimization techniques

The most important step in a removal process for pollutants is to increase the efficiency of the process via modeling and optimization without increasing the costs [111]. Because the removal processes involve interactions of variables and non-linear behavior, it is highly important that optimum experimental conditions are determined to obtain a maximum efficiency. High precision process optimization techniques based on AI approaches can be an effective solution in these processes [112,113]. AI tools have been broadly applied in various fields, for example, pattern recognition, autonomous driving, image understanding, big data, intelligent search, robotics, automatic programming, and human–computer game, consequently they will significantly impact the human society. AI tools mainly encompass artificial neural networks (ANNs) (Fig. 5), genetic algorithm (GA), immune algorithm, particle swarm optimization, support vector machine, boosted regression tree, random forest (RF), recurrent neural network (Fig. 6), Monte Carlo simulation, ant colony algorithm, simulated annealing and imperialist competitive algorithm [2]. AI tools have also been combined with experimental design (e.g., response surface methodology and uniform design) in order to improve the precision of optimal solutions prediction. For ANNs as a main tool of AI, however, their models are merely a black box, which cannot well reveal the system information and has certain limitations, thus it is important to make this structure model transparent. Elmolla et al. [114] reported the implementation of ANN for the prediction and simulation of antibiotic degradation in aqueous solutions by the Fenton process. A three-layer back-propagation neural network was selected to model and predict the degradation of

amoxicillin, ampicillin, and cloxacillin in aqueous solutions in terms of COD removal. Heydari et al. [115] described that RF was used for modeling and optimization of the removal of methylene blue (MB) and Pb^{2+} ion from aqueous solutions. In the training data set for MB and Pb^{2+} ion, the mean squared error of 0.0003 and 0.0002, and the determination coefficient (R^2) of 0.9952 and 0.9963 was obtained using the RF model, respectively. Additionally, the number of training sets is highly important for modeling (Fig. 4). Eslamian and Lavaei [116] presented a hybrid approach to analyze the nitrate pollution based on an ANN and GA. This makes it possible to readily compute the amount of nitrate in different time-scales. The results showed that the methods could be useful for management purposes and also beneficial for the treatment of groundwater.

3.2. Adsorption isotherms

Adsorption isotherm models explain the distribution of molecules between the liquid and solid phases when the adsorption processes reach equilibrium states (Table 2). Fitting of the adsorption data to different isotherm models is an important step in finding a suitable model that can be used for design purposes [60]. The Langmuir model indicates a monolayer coverage on the surface of the adsorbent, and the Freundlich model is indicative of surface heterogeneity of the adsorbent [127]. The Temkin isotherm describes the behavior of adsorption on a heterogeneous surface, and the derivation of the Temkin isotherm assumes that the fall in the heat of adsorption is linear rather than logarithmic [60]. The D–R model can determine the type of sorption (physical or chemical) [128]. Redlich–Peterson model is the widely used isotherm to represent the solute uptake process at equilibrium conditions [129,130]. The Flory–Huggins model was chosen to account for the degree of surface coverage characteristics of the sorbate on the sorbent [131]. Halsey proposed an expression for condensation of a multilayer process at a relatively large distance from the surface. And the Harkins–Jura adsorption isotherm also accounts for multilayer adsorption and explains the existence of a heterogeneous pore distribution [131].

3.3. Analysis of removal kinetics

In order to develop a working model for a reactor, it was considered necessary to perform a removal process in kinetics viewpoint (Table 3). The pollutants removal kinetics data were processed to calculate rate constants of the removal

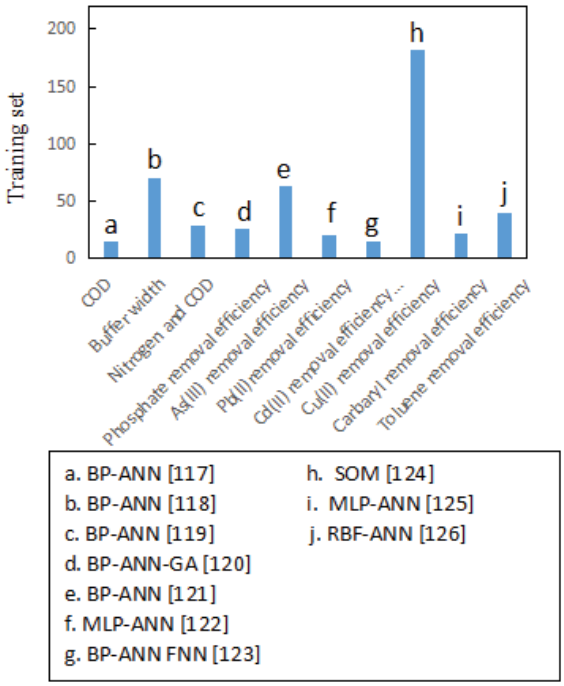

Fig. 4. Data rows of training sets used in different AI technologies.

Table 2
Adsorption isotherms

Materials	Pollutants	Types of adsorption	Isotherm models	References
Magnetic graphene/iron oxides composite	U(VI) ions from aqueous solutions	Langmuir adsorption	$q_e = \frac{q_m K_L C_e}{1 + K_L C_e}$	[129]
Graphene-supported nanoscale zero-valent iron	Phosphorus from synthetic rainwater runoff	Freundlich adsorption	$q_e = K\left(C_e\right)^{\frac{1}{n}}$	[127]
Reduced graphene oxide-iron oxide hybrid materials	Pb(II) from aqueous solutions	Temkin isotherm	$q_e = B\ln\left(AC_e\right)$	[60]
NiO/graphene nanosheets adsorbent	Congo Red azo-dye from aqueous solution	Redlich–Peterson model	$q_e = \frac{AC_e}{1 + BC_e}$	[132]
Hyperbranched polyamine functionalized graphene	Pb(II) from aqueous solutions	Redlich–Peterson isotherm	$q_e = \frac{AC_e}{1 + BC_e}$	[3]
	Methylene blue from aqueous solutions	Dubinin–Radushkevich (D–R) isotherm	$\ln q_e = \ln q_m - \beta\varepsilon^2$	[3]

Table 3
Kinetics models

Kinetics model	Physical/chemical/kinetic circumstances	Equation	References
Pseudo-first order	Adsorption equilibrium time was 60 min for Cr(VI) and 100 min for Cu(II) on three kinds of MRGO	$\ln(q_e - q_t) = \ln q_e - k_1 t$ where q_e is the amount of ions adsorbed per unit mass of adsorbents at equilibrium (mg/g), and q_t is the amount of ions adsorbed at time t (mg/g). The parameter k_1 represent the pseudo-first order constants of the kinetics models	[134]
Pseudo-second order	The work discusses the removal of crystal violet dye from aqueous solution by ultrasound-assisted adsorption using zinc oxide nanorods loaded on activated carbon as an adsorbent	$\frac{t}{q_t} = \frac{1}{k_2 q_e^2} + \frac{t}{q_e}$ where q_e is the amount of ions adsorbed per unit mass of adsorbents at equilibrium (mg/g), and q_t is the amount of ions adsorbed at time t (mg/g). k_2 represents the pseudo-second order rate constants of the kinetics models	[135]
Elovich equation	Congo Red azo-dye from aqueous solution of NiO/graphene nanosheets adsorbent. In addition, absorption spectra of a solution of Congo Red (20 mg/L, 100 mL) in the presence of NGNS-5 (50 mg) at different times	$q_t = A + 2.303B \log t$ where q_t is the amount of sorbate per unit mass (mg/g) of sorbent at time t (min), and A and B are Elovich constant	[132]
Morris–Weber equation		$q_t = R_{id} \times \sqrt{t} + c_t$ where q_t is the sorption capacity at equilibrium (mg/g) at time t (min) and R_{id} is the rate constant of intra-particle transport	[132]
Bangham model	Fabrication of hyperbranched polyamine functionalized graphene for high-efficiency removal of Pb(II) and methylene blue. (m = 10 mg, C_0 = 60 mg L^{-1}, V = 50 mL, pH at 6.1, temperature at 298 K) and MB (m = 10 mg, C_0 = 60 mg L^{-1}, V = 50 mL, pH at 5.9, temperature at 298 K	$\ln q_t - \ln k_b + \left(\frac{1}{m}\right)\ln t$ where q_t (mg/g) is the amounts of pollutants adsorbed onto the adsorbent at time t (min), m and k_b are the related constants of the Bangham model	[3]
Intraparticle diffusion model		$q_t = k_{id} t^{1/2} + C$ where k_{id} (mg/g/min$^{1/2}$) is the intraparticle diffusion rate constant	[3]

processes [133]. To examine the adsorption mechanism involved during the pollutants elimination processes, various kinetic models were tested, such as pseudo-first order, pseudo-second-order, the Elovich and the Morris–Weber models [132].

The pseudo-first order kinetics equation describes liquid–solid phase adsorption systems, which is the earliest known kinetics model describing the adsorption rate based on the adsorption capacity. The pseudo-second-order kinetics model is used to describe chemisorption, as well as cation exchange reactions. The Elovich equation was also employed to describe the chemisorption kinetics, which were useful in covering a wide range of slow adsorption. The Morris–Weber equation is generally applied to evaluate the intraparticle rate constant [132]. The Bangham kinetics model can be adopted to explain pore diffusion processes.

3.4. Error analysis

To determine the validity of isotherm and kinetics models, statistical analysis was carried out. In all regression cases, four different error functions (i.e., the sum of the square of the error (SSE), sum of absolute error (SAE), chi-square (χ^2), and standard deviation (SD)) between the experimental data and calculated values were evaluated using the equations in Table 4.

3.5. Thermodynamic studies

Thermodynamic models are powerful tools to describe metal sorption processes and explore the governing mechanisms. Thermodynamic parameters, for example, free energy changes ($\Delta G°$, kJ/mol), enthalpy changes ($\Delta H°$, kJ/mol), and entropy changes ($\Delta S°$, J/mol/K) are determined by the following equations [137,138]:

Table 4
Error analysis

Error analysis	Equation	Description	Reference
χ^2	$x^2 = \sum_{i=1}^{n}\left[\frac{\left(q_{e,\exp}-q_{e,\mathrm{cal}}\right)^2}{q_{e,\mathrm{cal}}}\right]_i$	where $q_{e,\exp}$ and $q_{e,\mathrm{cal}}$ stand for the experimental and calculated adsorption capacity (mg g^{-1}) and n represents the number of measurements	[136]
SSE	$\mathrm{SSE} = \sum_{i=1}^{n}\left(q_{e,\mathrm{cal}}-q_{e,\exp}\right)_i^2$		[136]
SAE	$\mathrm{SAE} = \sum_{i=1}^{n}\left\lvert q_{e,\exp}-q_{e,\mathrm{cal}}\right\rvert_i$		[96]
SD	$\mathrm{SD} = \sqrt{\frac{\left[\left(q_{e,\exp}-q_{e,\mathrm{cal}}\right)/q_{e,\mathrm{cal}}\right]^2}{n-1}}\times 100$		[96]

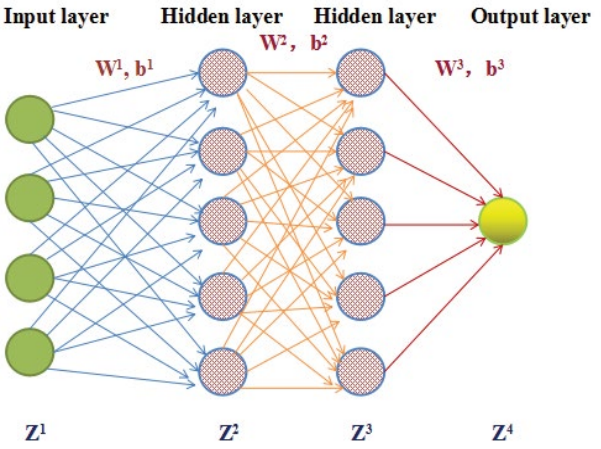

Fig. 5. Structure of a back-propagation artificial neural network.

$$\ln K_T = \frac{\Delta S^\circ}{R} - \frac{\Delta H^\circ}{RT} \quad (1)$$

$$\Delta G^\circ = -RT\ln K_T \quad (2)$$

$$K_T = \frac{C_0}{C_e} \quad (3)$$

where C_e (mg/L) stands for the equilibrium concentration of a pollutants in the solution, R (J/mol/K) is the gas constant (8.314), T (K) represents the absolute temperature, and K_e (L/g) is the removal equilibrium constant. Positive ΔH° values indicate that the removal process is endothermic, supported by a rise in q_e (mg/g) with increasing temperature. Negative ΔG° values suggest a spontaneous sorption process with increasing metal sorption at higher temperatures. Positive values of ΔS° may reflect an affinity of the graphene-supported iron-based composites for the pollutants. ΔG° (kJ/mol) could also provide information to distinguish between physicosorption and chemisorption processes [138,139].

4. Applications of graphene-supported iron-based composites in the removal of pollutants

A variety of graphene-supported iron-based composites were applied in the removal of pollutants, such as Fe_3O_4/GO, $CuFe_2O_4$@graphene, Fe_3O_4/Mn_3O_4-RGO, and Fe_3O_4@SiO_2-chitosan/GO. The application of different graphene-supported iron-based composites in the removal of pollutants is shown in Table 5. These graphene-supported iron-based composites gave high removal efficiencies for organic pollutants (such as $CuFe_2O_4$@graphene, GO–Fe_3O_4–Hb, $ZnFe_2O_4$-G, GFC hybrids, α-FeOOH/RGO, rGO/SnS_2/$ZnFe_2O_4$, and Fe_3O_4/Mn_3O_4-RGO) and for heavy metals (such as RGO-MFT, nZVI/rGO, AMGO, Fe_3O_4-CS-GO, Fe_3O_4@SiO_2@CS-TETA-GO, EDTA-mGO, RGO–ZNF–PANI, and Fe-PANI-GA).

4.1. Organic pollutants removal

The removal of various organic pollutants was carried out by different materials. Fe_3O_4/Mn_3O_4-RGO composites were employed for the degradation of sulfamethazine [83], which indicated that the removal efficiency of sulfamethazine was approximately 98% at following optimal conditions: pH = 3, T = 35°C, Fe_3O_4/Mn_3O_4-RGO composites = 0.5 g/L, H_2O_2 = 6 mM. Huang [67] reported the adsorption of TC on Fe_3O_4@SiO_2-chitosan/GO, and indicated that the highest adsorption capacity was 183.47 mmol/kg, and the experimental data well fitted to the pseudo-second-order kinetics model and Freundlich isotherm. Zhu et al. [147] studied the electro-enzymatic degradation of carbofuran with the GO–Fe_3O_4–Hb composites [85]. It was found that under the optimal conditions, the highest removal efficiency was 94.6% obtained after 40 min degradation through the electro-enzymatic treatment. The ternary graphene–TiO_2–Fe_3O_4 (GTF) nanocomposites were utilized for the removal of RhB by Lin [88]. They indicated that the GTF nanocomposite could work well in different pH environments and is capable of eliminating mixtures of various dyes. The graphene oxide-Fe_3O_4 nanocomposites (GO-Fe_3O_4) were explored for its surface adsorptive properties by employing a model organic compound, 2,4-dichlorophenoxy acetic acid (2,4-D) from aqueous

Table 5
Applications of different graphene-supported iron-based composites in the pollutants removal from wastewater

Materials	Pollutants	Operating parameters	Results	References
M-G/C	As(III) and As(V)	Initial concentration	Arsenic adsorption quantity by M-G/C increased from 3.89 to 9.11 mg/g for As(III) and from 2.76 to 5.21 mg/g for As(V), respectively, when the initial concentration was increased from 1 to 5 mg/L	[140]
PG-Fe_3O_4	As(III) and As(V)	pH and temperature	PG-Fe_3O_4 hybrid composite has large surface adsorption sites and exhibits high adsorption capacities of 104 mg/g for As(III) and 68 mg/g for As(V) at 25°C and pH 7	[44]
RGO-MFT	As(III) and As(V)	Time and pH	Equilibrium adsorption was attained within 15 min for both As(III) and As(V). The maximum adsorption capacity for As(V) and As(III) was found to be 99.5 and 77.7 mg/g at pH 6 and 7, respectively	[62]
MGL	Arsenate	Time, concentration of arsenate and pH	Adsorption data are better fitted by the Langmuir model rather than by the Freundlich model. The calculated values of q_{max} is 73.14 mg/g for MGL	[92]
$CuFe_2O_4$@ graphene	Alizarine yellow (AY)	Adsorbent mass, pH, ionic strength and contact time	AY could be effectively removed from aqueous solution by $CuFe_2O_4$@ graphene composites within 40 min of contact time and pH 3, and the adsorption capacity of $CuFe_2O_4$ is 145 mg/g for AY	[59]
Fe_3O_4/rGO	Ametryn, prometryn, simazine, simeton and atrazine	Time, pH and ionic strength	Adsorption isotherm studies show that the maximum adsorption capacity of 54.8 mg/g is achieved at pH 5 and it was enhanced in the presence of different ions (Mg^{2+}, Ca^{2+}, Na^+ and SO_4^{2+}) and maximum (63.7 mg/g) for ametryn adsorption was found in seawater medium	[141]
GO–Fe_3O_4–Hb	Carbofuran	Removal time and immobilized Hb dose	Removal efficiency of carbofuran reached 94.6% under the optimum conditions	[85]
nZVI/rGO	Cd(II)	Cd(II) concentration, temperature, pH and contact time initial	ANN predicted Cd(II) removal at the GA optimized condition was 81.50% at the condition of 20.16 mg/L, 6.48, 30.00 min, and 25.31 C. This result was cross-validated by performing batch experiments at the GA-specified optimum condition. The removal of Cd(II) achieved during experimental condition was 82.38% ± 0.82%, which was in a good agreement with the ANN-GA prediction	[142]
SGO/Fe-Mn-am SGO/Fe-Mn-ac SGO/Fe-Mn-ne	CH_3Hg^+	pH, dissolved organic matter, temperature, ionic strength, and time	Maximum sorption capacity of CH_3Hg^+ by SGO/Fe-Mn-am, SGO/Fe-Mn-ac, and SGO/Fe-Mn-ne are 43.88, 36.33, and 28.00 mg/g, separately	[7]
Fe_3O_4/GO MNPs	2-Chlorophenol 4-chlorophenol 2,4-dichlorophenol	Temperature, reaction time, immobilized enzyme dosage, and initial pH	Order of the chlorophenol removal efficiencies was 2-chlorophenol < 4-chlorophenol < 2,4-dichlorophenol	[71]
$ZnFe_2O_4$-G	MB	H_2O_2 concentrations, temperature and Time	It was found that in the presence of H_2O_2, the photodegradation rate of methylene blue (MB) was 88% after visible light irradiation for only 5 min and reached up to 99% after irradiation for 90 min	[90]

(Continued)

Table 5 Continued

Materials	Pollutants	Operating parameters	Results	References
Fe_3O_4-GN nanocomposites	MB	Time and initial mass ratio of the Fe_3O_4 quantum dots and GN	Fe_3O_4-GN nanocomposites (Fe_3O_4:GN = 1:5) exhibited excellent adsorption ability in the removal of MB dyes	[35]
GFC hybrids	MB	Contact time	MB adsorption increases as the adsorption time increases and the MB removal efficiency of GFC reaches 97.8% after equilibrium adsorption	[143]
α-FeOOH/RGO	Methyl orange (MO)	Temperature, time	Catalyst showed a high catalytic activity and a 1 mmol/L (1.330 mg/L) solution of MO was almost 100% discolored in 24 h	[39]
rGO/SnS_2/$ZnFe_2O4$	2-Nitrophenol	Time, temperature	rGO/SnS_2/$ZnFe_2O_4$ composite demonstrated the highest visible-light photocatalytic activity with almost 100% 2-nitrophenol removal	[41]
nZVI/rGO	Pb(II)	Time, pH, initial concentration and temperature	Process optimization modeling indicated that the optimal parameters (T = 21.30°C, pH = 5.00, C = 400.00 mg/L and t = 60.00 min) gave the 100.37% removal percentage for Pb(II) ions, which is satisfactory though with a certain amount of error. The relative error between average removal percentage obtained through confirmation experiments and the predicted value of the model was within 5%. It should be noted that the optimal value was valid within the specified range of process	[107]
GO–$MnFe_2O_4$ hybrid	Pb(II), As(V) and As(III)	pH, temperature and competing ions	Maximum adsorption occurs at pH = 5 for Pb(II), pH = 4 for As(V) and pH = 6.5 for As(III); The adsorption of both lead as well as arsenic was found to increase with increase in temperature; the study for the effect of competing ions showed that NO_3^-, SO_4^{2-}, Cd^{2+}, and Zn^{2+} ions have much less effect on the adsorption capacity, whereas HCO_3^- and HPO_4^{2-} decrease the adsorption capacity to a large extent	[144]
$MnFe_2O_4$-G	Pb(II) and Cd(II)	Temperature time and pH	Adsorption of Pb and Cd ions increased and reached equilibrium within 120 and 180 min at 37°C with a maximum adsorption at pH 5 and 7, respectively	[87]
nZVI/rGO	Rh B	Initial pH, initial concentration, time and temperature	Effects of several important parameters on the removal were optimized by response surface methodology (RSM) and artificial neural network hybridized with genetic algorithm (ANN-GA). The results suggest that the ANN-GA model was more accurate than the RSM model. The predicted optimum value of Rh B removal efficiency (90.0%) was determined using the ANN-GA model, which was compatible with the experimental value (86.4%)	[145]
Fe_3O_4@SiO_2-Chitosan/GO	Tetracycline (TC)	pH, zeta potential, and initial contaminant concentration	Highest adsorption capacity of TC was 183.47 and 67.57 mmol/kg on Fe_3O_4@SiO_2^- chitosan/GO with and without Cu(II)	[67]
EDTA-mGO	U(VI)	Temperature, contact time, and pH.	EDTA-mGO showed fast removal capacity for U(VI) (<1.5 h) with high sorption ability (277.43 mg/g)	[99]
RGO–ZNF–PANI	U(VI)	pH and temperature	Maximum adsorption capacity of uranium with the RGO–ZNF–PANI composite was 1,885 mg/g at pH 5 and 25°C	[21]
Fe-PANI-GA	U(VI)	pH, shaking time, U(VI) concentration, and temperature	Results also showed that the maximum removal capacity of the Fe-PANI-GA toward U(VI) was 350.47 mg/g at pH 5.5	[146]

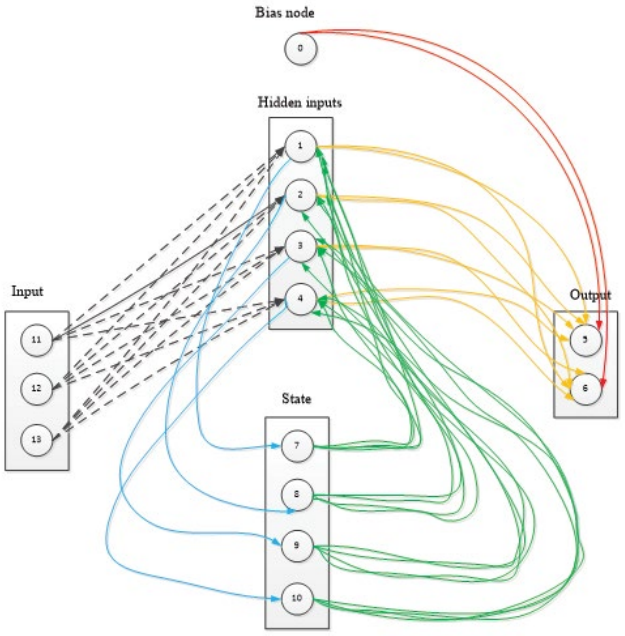

Fig. 6. Structure of recurrent neural network.

solutions [148]. This shows that the maximum monolayer capacity from Langmuir isotherm is 67.26 mg/g. Kinetic studies were also performed and the studied adsorption process followed pseudo-second-order rate equation. Tran et al. [149] investigated the potential of chitosan/Fe_3O_4/graphene oxide (CS/Fe_3O_4/GO) nanocomposites for the efficient removal of methylene blue (MB) from aqueous solutions. Their results showed that the adsorption equilibrium data were fitted well to the Langmuir isotherm rather than Freundlich isotherm, and the maximum monolayer capacity (q_{max}) was calculated from the Langmuir model as 30.10 mg/g.

Magnetic graphene–Fe_3O_4@carbon (GFC) hybrids were successfully prepared via a facile method [143]. In this work, the adsorption performance for removing organic dyes was also investigated, and approximately 40% improvement was shown in comparison with the corresponding binary graphene–Fe_3O_4 and Fe_3O_4@carbon hybrids. The hybridization of the graphene sheets and the amorphous carbonaceous shells greatly enhances the specific surface area, which provides more active sites for MB adsorption. The graphene-based composites with γ-Fe_2O_3 nanoparticles were employed for the removal of endocrine-disrupting compounds (EDCs) from water [150]. The adsorption equilibrium data were well fitted to the Langmuir model, and the maximum adsorption capacities for 1-naphthol and bisphenol A were determined as 680 and 360 mg/g, respectively. Deng et al. [41] investigated the photocatalytic removal of 2-nitrophenol by rGO/SnS_2/$ZnFe_2O_4$. Their results disclosed that the photocatalytic activity of rGO/SnS_2/$ZnFe_2O_4$ was influenced by rGO content, the optimal rGO content is 7%, and the enhanced photocatalytic activity of rGO/SnS_2/$ZnFe_2O_4$ composites could be attributed to the high adsorption rate. The $ZnFe_2O_4$-G nanocomposites were adopted as photoelectrochemical degrader for methylene blue removal [90]. It was demonstrated that the $ZnFe_2O_4$-G catalyst had an important dual function as the photoelectrochemical degrader. The strong oxidant hydroxyl radical was generated via photoelectrochemical decomposition of H_2O_2 under visible light irradiation. Hashemian et al. [59] studied the removal of AY by $CuFe_2O_4$@graphene nanocomposites. Their results indicated that the adsorption process was very fast and reached the adsorption equilibrium within 40 min of contact time. The $ZnFe_2O_4$@CS/GO composites were utilized for the adsorption of BF [151], which showed that there were strong electrostatic interactions between BF and $ZnFe_2O_4$@CS/GO. This adsorption followed pseudo-second-order kinetics, and the equilibrium data were modeled well by the Langmuir isotherm. Reduced graphene oxide decorated with $MnFe_2O_4$ ($MnFe_2O_4$-G) composites were applied in the removal of glyphosate [152]. It was illustrated that the maximum adsorption capacity was 39 mg/g at 5°C and low temperature was determined to be favorable for the adsorption.

Chemical oxidation technology has a remarkable effect on the treatment of toxic and organic pollutants in wastewater. The advanced oxidation processes (AOP) is one of the most effective chemical oxidation technologies and plays an important role in the treatment of wastewater. In AOPs, the reaction follows a unique oxidation pathway, usually including the formation of highly active free radicals, such as $^{\bullet}OH$ or $^{\bullet}SO_4^-$. These free radicals have a high chemical activity (E^0 $^{\bullet}OH$ = 2.8 V, E^0 $^{\bullet}SO_4^-$ = 2.6 V). They can easily interact with organic molecules to destroy their structures and achieve the effect of pollutants removal. Graphene-supported iron-based composites have been employed for activating potassium persulfate. Yao [153] reported magnetic recoverable $MnFe_2O_4$ and $MnFe_2O_4$-graphene hybrid as heterogeneous catalysts of peroxymonosulfate activation for efficient degradation of organic pollutants in aqueous solutions.

$$\equiv Mn(II) - {}^{-}OH + HSO_5^- \rightarrow \equiv Mn(III) - {}^{-}OH + SO_4^{-\bullet} \quad (4)$$

$$\equiv Mn(III) - {}^{-}OH + HSO_5^- \rightarrow \equiv Mn(II) - {}^{-}OH + SO_5^{-\bullet} + H^+ \quad (5)$$

$$\equiv Fe(II) - {}^{-}OH + HSO_5^- \rightarrow \equiv Fe(III) - {}^{-}OH + SO_4^{-\bullet} + OH^- \quad (6)$$

$$\equiv Fe(III) - {}^{-}OH + HSO_5^- \rightarrow \equiv Fe(II) - {}^{-}OH + SO_5^{-\bullet} + H^+ \quad (7)$$

4.2. Heavy metals removal

The various graphene-supported iron-based composites have been extensively applied in the removal of different heavy metals. The graphene/Fe_3O_4 composites were employed for removal of Zn(II) and Ni(II) ions by Muthukrishnaraj et al. [154] and Manokaran [60]. It was indicated that the maximum removal percentage of Zn(II) and Ni(II) ions were 96% and 87%, respectively, which were achieved under the conditions of pH of 7, adsorbent dosage of 0.3 g/L, metal ion concentration of 30 mg /L, time of 60 (min) and temperature of 303 K. Dat et al. [155] studied the removal of U (VI) by reduced graphene oxide–$Zn_{0.5}Ni_{0.5}Fe_2O_4$ ferrite–polyaniline (RGO–ZNF–PANI) composites. This adsorption process was completed within 240 min and could be well described by the pseudo-second-order model, and the equilibrium data were well fitted to the Langmuir adsorption isotherm [21]. The same element was removed by a regenerable magnetic

ligand material (EDTA-mGO) [99], and it was demonstrated that the highest sorption capacity was 277.43 mg/g, 2–3 times higher than that of mGO. $MnFe_2O_4$-G composites were used for removing Pb(II) and Cd(II) ions [87]. The Langmuir model for this removal process correlates to the experimental data showing an adsorption capacity of 100 mg/g for Pb(II) and 76.90 mg/g for Cd(II). The novel nanocomposites of xanthated Fe_3O_4-chitosan grafted onto graphene oxide (xanthated Fe_3O_4-CS-GO) were utilized for the removal of Cu(II) from aqueous solutions [156]. These nanocomposites were found to adsorb Cu(II) effectively and to be relatively environmentally benign, easy to recover, and convenient to use in practice. The magnetic Fe_3O_4/GO composites were adopted as a sorbent for the removal of Cr(VI) ions from water [8], and a high sorption capacity was obtained (32.33 mg/g). Li et al. [45] described the mechanism of magnetic Fe_3O_4/SiO_2–GO nanocomposites for Cr(III) removal as shown below.

- Cr(III) reacts with –COOH and –OH groups on GO surface to form a complex

$$GO–COOH + Cr^{3+} \rightarrow GO–COO^––Cr^{3+} + H^+$$
$$(GO–COOH)_2 + Cr^{3+} \rightarrow (GO–COO^–)_2–Cr^{3+} + 2H^+$$
$$(GO–COOH)_3 + Cr^{3+} \rightarrow (GO–COO^–)_3–Cr^{3+} + 3H^+$$
$$GO–OH + Cr^{3+} \rightarrow GO–O^––Cr^{3+} + H^+$$
$$(GO–OH)_2 + Cr^{3+} \rightarrow (GO–O^–)_2–Cr^{3+} + 2H^+$$
$$(GO–OH)_3 + Cr^{3+} \rightarrow (GO–O^–)_3–Cr^{3+} + 3H^+$$

- Cr(III) may also react with –OH groups of Fe_3O_4/SiO_2 to form a complex

$$Fe_3O_4/SiO_2–OH + Cr^{3+} \rightarrow Fe_3O_4/SiO_2–O^––Cr^{3+} + H^+$$
$$(Fe_3O_4/SiO_2–OH)_2 + Cr^{3+} \rightarrow (Fe_3O_4/SiO_2–O^–)_2–Cr^{3+} + 2H^+$$
$$(Fe_3O_4/SiO_2–OH)_3 + Cr^{3+} \rightarrow (Fe_3O_4/SiO_2–O^–)_3–Cr^{3+} + 3H^+$$

Babu et al. [62] investigated the removal of As(III) and As(V) by the reduced graphene oxide supported mesoporous Fe_2O_3/TiO_2 (RGO-MFT). It was demonstrated that the adsorption at pH = 6 was found to be better than at higher pH [62]. The same pollutants were removed by PS@+rGO@GO@Fe_3O_4 (PG-Fe_3O_4) hybrid composites, indicating that these composites had a high adsorption capacity of 104 mg/g for As(III) and 68 mg/g for As(V) at 25°C and pH = 7 [44]. Huang et al. [7] demonstrated the removal of CH_3Hg^+ by SGO/Fe-Mn-am, SGO/Fe-Mn-ac, and SGO/Fe-Mn-ne. Their results showed that SGO/Fe-Mn-am prepared via ammonium hydroxide method possessed a high maximum sorption capacity. The applications of different graphene-supported iron-based composites in the removal of heavy metals shown in Table 6. The results showed that the removal capacity of heavy metals for iron-based materials was significantly higher than that of non-iron-based materials.

5. Regeneration and reusability of graphene-supported iron-based composites

It is well known that the stability and regeneration ability of the composites during the removal processes is crucial to its practical applications. Good composites should possess a high removal capability as well as a good desorption property [159–161]. Many researchers carried out the studies on regeneration experiments of graphene-supported iron-based composites (Table 7). The number of cycles is more than three for pollutants removal by GO-Fe_3O_4, CS/Fe_3O_4/GO, $ZnFe_2O_4$-G, Fe/Fe_3C@Fe/N-graphene, Fe_3O_4/Mn_3O_4-RGO, EDTA-mGO, GO-$MnFe_2O_4$, and Fe_3O_4@SiO_2-chitosan/GO. The removal efficiency of pollutants by all graphene-supported iron-based composites can still reach more than 80% after several cycles.

6. Ecotoxicological studies

The production and use of engineered nanomaterials have grown rapidly, and therefore the presence of these materials seems inevitable in the environment [162]. Their potential toxicity for humans and animals is yet to be understood, thus the studies on environmental behavior, fate, bioavailability, and ecotoxicological effects of engineered nanomaterials have been conducted extensively in the recent years [163]. Nanoparticles show some complex colloid and aggregation chemistry, which is likely to be affected by their particle shape, size, surface area and surface charge, and adsorption properties. Abiotic factors such as pH, ionic strength, water hardness, and the presence of organic matter can alter aggregation chemistry; and are expected to influence toxicity [164]. The physico-chemistry is essential to understanding of the fate and behavior of nanoparticles in the environment, uptake and distribution within organisms, and the interactions of nanoparticles with other pollutants. Data concerning biological effects show that nanoparticles can be toxic to bacteria, algae, invertebrates, fish species, as well as mammals. And the environmental risk assessment of nanomaterials could be performed using the existing tiered approach and regulatory framework [164].

The fate and toxicity of nanoparticles including graphene-based nanomaterials can be influenced by many factors, for example, chemical composition, physical, and chemical transformation (abiotic/biotic) in the environment [165]. Temsah and Joner [167] studied the ecotoxicological effects of NZVI coated with carboxymethyl cellulose on *Eisenia fetida* and *Lumbricus rubellus*. This work proved the negative impact of NZVI on both of these earthworm species by affecting the reproduction. The NZVI concentration reached 100 mg/kg leading to a decreased weight while the concentrations above 500 mg/kg caused an increased mortality rate [166,167]. For the soil evaluation, the studies are often focused on the sensibility of earthworms and the germination test of *Lactuca sativa*. For the water evaluation, daphnia is used as the test organism [168]. NZVI can affect the germination of plants and can lead to the death of earthworms with high dose, and the uptake of NZVI by the roots and leaves of plants have been confirmed. The experimental results showed that NZVI could also endanger organisms with only a few nanograms per liter, for example, prokaryotes, invertebrates, and fish [163,166].

7. Conclusions

In this paper, we have reviewed the present progress in the synthesis and characterization of graphene-supported iron-based composites, and their applications in wastewater treatment. Iron-based materials (e.g., Fe^0, Fe_3O_4, Fe_2O_3, $MnFe_2O_4$, $CuFe_2O_4$, $CoFe_2O_4$, $NiFe_2O_4$, and $ZnFe_2O_4$) have been widely used in wastewater treatment due to strong

Table 6
Pollutants removal by different adsorbents

Materials	Pollutants	Operating parameters	Results	References
AMGO	Cr(VI)	Time, temperature and pH	Maximum adsorption capacity of the AMGO for Cr(VI) was 123.4 mg/g, displaying a high efficiency for the removal of Cr(VI)	[89]
G-nZVI	Cr(VI)	pH, initial Cr(VI) concentration, time	Maximum adsorption capacity is 162 mg/g.	[157]
Fe_3O_4/GO	Cr(VI)	pH and temperature	Maximum sorption capacity for Cr(VI) on Fe_3O_4/GO was 32.33 mg/g	[8]
Fe_3O_4-CS-GO	Cu(II)	Cu(II) concentration, temperature, time and pH	Maximum Cu(II) adsorption capacity of the xanthated Fe_3O_4-CS-GO was 426.8 mg/g	[156]
nZVI/rGO	Cu(II)	Cu(II) concentration, temperature, initial pH, and contact time	Using the ANN-PSO based tool, the Cu(II) removal efficiency from aqueous solutions was improved by 3.15% and 8.54% as compared with that of the ANN-GA model and the RSM model. The high removal efficiency and low absolute error of the ANN-PSO model indicated that this model was proven to be an alternative for modeling and optimizing the Cu(II) removal process	[158]
Fe_3O_4@SiO_2@ CS-TETA-GO	Cu(II), MB	Initial concentration and pH	Maximum adsorption capacity was about 324.7 mg g^{-1} for Cu(II) in 16 min and 529.1 mg g^{-1} for MB in 20 min	[4]
GO-Fe_3O_4	2,4-Dichlorophenoxy acetic acid (2,4-D)	Adsorbent dosage and initial adsorbate concentration	Effect of adsorbent dosage was studied by varying the GO-Fe_3O_4 dosage from 0.1 to 0.5 g. The percentage adsorption increases with the increase in the adsorbent dosage. And the effect of initial adsorbate concentration was also studied by varying the 2,4-D concentration from 50 to 750 mg/L. The percentage adsorption decreases with the increase in the adsorbate concentration	[148]
$MnFe_2O_4$-G	Glyphosate	Temperature	Maximum adsorption capacity was 39 mg/g at 5°C	[152]
nZVI/rGO	Rh B	Initial pH, initial concentration, time, and temperature	Effects of several important parameters on the removal were optimized by response surface methodology (RSM) and artificial neural network hybridized with genetic algorithm (ANN-GA). The results suggest that the ANN-GA model was more accurate than the RSM model. The predicted optimum value of Rh B removal efficiency (90.0%) was determined using the ANN-GA model, which was compatible with the experimental value (86.4%)	[145]
Fe/Fe_3C@ Fe/N-Graphene	Rh 6G	Catalyst dosage, H_2O_2 dosage, and time	Removal efficiency was 61.8%	[101]
nZVI/rGO	Se(IV)	Initial pH, initial concentration, time, and temperature	Removal efficiency was 90.89% under the optimized conditions from ANN-GA model (T = 29.65°C, initial pH = 6.55, C = 36.13 mg/L, and t = 64.22 min). The removal efficiency from the confirmatory experiment was 88.01%, and the residual error between the predicted and experimental values was 2.88%, confirming that ANN-GA model is feasible for modeling and optimizing the Se(IV) removal by the nZVI/rGO composites	[113]
Fe_3O_4/Mn_3O_4-RGO	Sulfamethazine (SMT)	SMT concentration, H_2O_2 concentration, pH, catalyst dosage, and temperature	SMT degradation experiments under different conditions Showed that 98% degradation rate was achieved under optimal conditions	[83]
Graphene/Fe_3O_4 composite	Zn(II) and Ni(II) ions	pH, initial metal ion concentration, time adsorbent dosage, and temperature	Maximum adsorption capacity of the GFC adsorbent toward Zn(II) and Ni(II) ions was found to be 121.5 and 111.4 mg g^{-1}, respectively	[60]

Table 7
Regeneration studies of different graphene-supported iron-based composites

Materials	Removed pollutants	Cycle times	Results after cyclic removal	References
GO-$MnFe_2O_4$	Arsenic	5	Arsenic removal efficiency decreased from 99.9% to 83.6%	[81]
RGO-MFT	As(V) and As(III)	4	Adsorption capacity decreased by 7%–8% for the first regeneration, and decreased by less than 3% for further three cycles	[62]
Fe_3O_4/rGO	Ametryn	7	Fe_3O_4/rGO nanocomposites can be reused up to seven times without any significant loss of its adsorption capacity	[141]
GO–Fe_3O_4–Hb	Carbofuran	6	Removal efficiency of GO–Fe_3O_4–Hb composites decreased with the increase of the number of cycles, and the composites could still remove 64% carbofuran after six cycles	[85]
Xanthated Fe_3O_4-CS-GO	Cu(II)	5	Adsorption capacity was slightly lower after each cycle because the Cu(II) was incompletely desorbed, but the adsorption capacity remained good even after five cycles	[156]
AMGO	Cr(VI)	5	Adsorption capacity is 123.4 mg/g at the first cycle and then slightly deceased to 106.5 mg/g at the fifth cycle	[89]
GO-Fe_3O_4	2,4-Dichlorophenoxy	3	GO-Fe_3O_4 nanocomposites regenerated using acetone was able to adsorb 91% of 2,4-D molecules from aqueous solution for the third cycle	[148]
GO/Fe_3O_4	2,4-Dichlorophenol	4	Catalytic activity of the recycled GO/Fe_3O_4 was still as high as 85% after four cycles	[33]
HRP immobilized on the Fe_3O_4/GO MNPs	2,4-Dichlorophenol	4	Immobilized HRP retains 66% of its initial activity for the first four cycles	[71]
CS/Fe_3O_4/GO	MB	6	Removal efficiency was 99.9% for the first time and decreased to 80.6% for the sixth time	[149]
$ZnFe_2O_4$-G	MB	10	Photodegradation rate of MB still reached over 95% after 10 cycles	[90]
GFC hybrid	MB	5	About 86% and 77% of the dye removal efficiency can be retained after five cycles in water and 1 M HCl, respectively	[143]
HRP immobilized on GO/Fe_3O_4	Phenol	4	Removal efficiency dropped to 40% of its initial activity after four cycles	[34]
GO-Fe_2O_3	RhB	7	GO-Fe_2O_3 catalyst did not exhibit any significant loss of photocatalytic activity after seven recycles	[31]
GTF	RhB	5	Photocatalytic activity of GTF was almost unchanged after reusage during five cycles	[88]
Fe/Fe_3C@Fe/N-Graphene	Rh 6G	13	Removal efficiency of Rh 6G was about 96% after 13 successive cycles	[101]
Fe_3O_4/Mn_3O_4-RGO	Sulfamethazine (SMT)	5	The catalyst was used for five times, which was washed with water after each use. The removal efficiency of SMT was 98%, 92.5%, 90 %, 86%, and 82%, respectively	[83]
Fe_3O_4@SiO_2-chitosan/GO	TC	5	At the fifth cycle, the adsorption capacity of TC with and without Cu(II) decreased to approximately 85.7%and 84.0% of the initial adsorption amounts, respectively	[67]
EDTA-mGO	U(VI)	5	Sorption efficiency of U(VI) onto the EDTA-mGO decreased from 91% to 81% after five cycles	[99]
Fe_2O_3-GO	U(VI)	4	Photocatalytic reduction efficiency of U(VI) decreased to 76.0% after four cycles	[86]
Fe-PANI-GA	U(VI)	5	Sorption capacity reduced from 144.2 to 127.3 mg/g for U(VI) after five successive sorption–desorption cycles and the decline was significant after recycle for five times (11.7%)	[146]

adsorption capability, high magnetism, strong reducibility, and good photocatalytic properties. However, some technical issues, for example, aggregation, poor stability, shortage of durability and mechanical strength, hinder the practical applications of iron-based materials. Especially, aggregation is hard to be avoided due to the magnetic interaction among the iron-based materials, hence the aggregation of iron-based materials could be reduced when they were supported on the graphene. In this way, their dispersion ability and specific surface area were improved and their reactivity was enhanced [169,170]. We have also summarized the adsorption isotherms, removal kinetics, thermodynamic studies, and AI-based optimization approaches for pollutants removal processes using these composites. It is of great significance to reduce costs by the reuse of graphene-supported iron-based composites. Future research should involve emerging two-dimensional materials for the removal of pollutants, for example, carbon nitride, boron nitride, molybdenum disulfide, borophene, and silylene. Mechanistic models and more advanced AI techniques can be applied based on the modeling and optimization of complex removal processes with the aid of experimental design (e.g., RSM and uniform design). In order to avoid secondary environmental pollution, the study on the ecotoxicology of nanomaterials should be further performed. In addition, a larger scale in-situ permeable reactive barrier system should be used to investigate the pollutants removal from wastewater, which can hopefully lead to practical applications.

Acknowledgments

This research was financially supported by the National Natural Science Foundation of China under Grants No. 21667012, 21367009 and the National 111 Project of China under Grant No. D17016.

References

[1] J. Liu, G. Liu, W. Liu, Preparation of water-soluble β-cyclodextrin/poly (acrylic acid) /graphene oxide nanocomposites as new adsorbents to remove cationic dyes from aqueous solutions, Chem. Eng. J., 257 (2014) 299–308.
[2] M. Fan, J. Hu, R. Cao, W. Ruan, X. Wei, A review on experimental design for pollutants removal in water treatment with the aid of artificial intelligence, Chemosphere, 200 (2018) 330–339.
[3] L. Hu, Fabrication of hyperbranched polyamine functionalized graphene for high-efficiency removal of Pb(II) and methylene blue, Chem. Eng. J., 287 (2016) 545–556.
[4] F. Wang, L. Zhang, Y. Wang, X. Liu, S. Rohani, J. Lu, Fe_3O_4@SiO_2@CS-TETA functionalized graphene oxide for the adsorption of methylene blue (MB) and Cu(II), Appl. Surf. Sci., 23 (2017) 420–431.
[5] V.M. Esquerdo, C.T. Jr, G.L. Dotto, L.A. Pinto, Chitosan scaffold as an alternative adsorbent for the removal of hazardous food dyes from aqueous solutions, J. Colloid Interface Sci., 424 (2014) 7–15.
[6] Z. Geng, Highly efficient dye adsorption and removal: a functional hybrid of reduced graphene oxide–Fe_3O_4 nanoparticles as an easily regenerative adsorbent, J. Mater. Chem., 22 (2012) 3527–3535.
[7] Y. Huang, J. Tang, L. Gai, Y. Gong, H. Guan, R. He, H. Lyu, Different approaches for preparing a novel thiol-functionalized graphene oxide/Fe-Mn and its application for aqueous methylmercury removal, Chem. Eng. J., 319 (2017) 229–239.
[8] M. Liu, T. Wen, X. Wu, C. Chen, J. Hu, J. Li, X. Wang, Synthesis of porous Fe_3O_4 hollow microspheres/graphene oxide composite for Cr(VI) removal, Dalton Trans., 42 (2013) 14710.
[9] R.X. Liu, R.J. Tan, B. Li, Y.H. Song, B. Zeng, Z.S. Li, Overview of POPs and heavy metals in Liao River Basin, Environ. Earth Sci., 73 (2015) 5007–5017.
[10] A. Demir, A. Gunay, E. Debik, Ammonium removal from aqueous solution by ion-exchange using packed bed natural zeolite, Water SA, 28 (2002) 329–335.
[11] Y. Masue, R.H. Loeppert, T.A. Kramer, Arsenate and arsenite adsorption and desorption behavior on coprecipitated aluminum:iron hydroxides, Environ. Sci. Technol., 41 (2007) 837–42.
[12] R.C. Cheng, S. Liang, H.C. Wang, M.D. Beuhler, Enhanced coagulation for arsenic removal, J. Am. Water Works Assoc., 86 (1994) 79–90.
[13] Y. Yoon, Y. Hwang, M. Ji, B. Jeon, J. Kang, Ozone/membrane hybrid process for arsenic removal in iron-containing water, Desal. Wat. Treat., 31 (2011) 138–143.
[14] P. Brandhuber, G. Amy, Arsenic removal by a charged ultrafiltration membrane-influences of membrane operating conditions and water quality on arsenic rejection, Desalination, 140 (2001) 1–14.
[15] A.I. Alonso, A.M. Urtiaga, S. Zamacona, A. Irabien, I. Ortiz, Kinetic modelling of cadmium removal from phosphoric acid by non-dispersive solvent extraction, J. Membr. Sci., 130 (1997) 193–203.
[16] H. Polat, D. Erdogan, Heavy metal removal from waste waters by ion flotation, J. Hazard. Mater., 148 (2007) 267–273.
[17] J. Ma, W. Liu, Effectiveness and mechanism of potassium ferrate (VI) preoxidation for algae removal by coagulation, Water Res., 36 (2002) 871–878.
[18] P. Gao, X. Chen, F. Shen, G. Chen, Removal of chromium(VI) from wastewater by combined electrocoagulation–electroflotation without a filter, Sep. Purif. Technol., 43 (2005) 117–123.
[19] C.T. Wang, W.L. Chou, Y.M. Kuo, Removal of COD from laundry wastewater by electrocoagulation/electroflotation, J. Hazard. Mater., 164 (2009) 81–86.
[20] A.L. Dolo, S. Goel, Effect of electrode combinations, pH and current density on arsenic removal from drinking water using electrocoagulation, J. Inst. Eng. Environ. Eng. Div., 25 (2010) 21–25.
[21] D.Q. Tran, H.T. Pham, H.Q. Do, Efficient removal of uranium from aqueous solution by reduced graphene oxide–$Zn_{0.5}Ni_{0.5}Fe_2O_4$ ferrite–polyaniline nanocomposite, J. Electron. Mater., 46 (2017) 3273–3278.
[22] W. Qi, Y. Zhao, X. Zheng, M. Ji, Z. Zhang, Adsorption behavior and mechanism of Cr(VI) using Sakura waste from aqueous solution, Appl. Surf. Sci., 360 (2016) 470–476.
[23] Y. Chen, H. Xu, S. Wang, L. Kang, Removal of Cr(VI) from water using polypyrrole/attapulgite core-shell nanocomposites: equilibrium, thermodynamics and kinetics, RSC Adv., 4 (2014) 17805–17811.
[24] Y. Zhao, D. Zhao, C. Chen, X. Wang, Enhanced photo-reduction and removal of Cr(VI) on reduced graphene oxide decorated with TiO_2 nanoparticles, J. Colloid Interface Sci., 405 (2013) 211–217.
[25] N. Kannan, M.M. Sundaram, Kinetics and mechanism of removal of methylene blue by adsorption on various carbons-a comparative study, Dyes Pigm., 51 (2001) 25–40.
[26] M. Doğan, M. Alkan, A. Türkyilmaz, Y. Ozdemir, Kinetics and mechanism of removal of methylene blue by adsorption onto perlite, J. Hazard. Mater., 109 (2004) 141–148.
[27] J. Aguado, J.M. Arsuaga, A. Arencibia, M. Lindo, V. Gascón, Aqueous heavy metals removal by adsorption on amine-functionalized mesoporous silica, J. Hazard. Mater., 163 (2009) 213–221.
[28] R.L. Johnson, Field-scale transport and transformation of carboxymethylcellulose-stabilized nano zero-valent iron, Environ. Sci. Technol., 47 (2013) 1573–1580.
[29] J. Li, C. Chen, K. Zhu, X. Wang, Nanoscale zero-valent iron particles modified on reduced graphene oxides using a plasma technique for Cd(II) removal, J. Taiwan Inst. Chem. Eng., 59 (2016) 389–394.
[30] M.A. Gondal, A. Hameed, Z.H. Yamani, A. Suwaiyan, Production of hydrogen and oxygen by water splitting using laser induced photo-catalysis over Fe_2O_3, Appl. Catal. A, 268 (2004) 159–167.

[31] S. Guo, G. Zhang, Y. Guo, J.C. Yu, Graphene oxide–Fe_2O_3 hybrid material as highly efficient heterogeneous catalyst for degradation of organic contaminants, Carbon, 60 (2013) 437–444.
[32] X.S. Lv, Y. Qiu, Z.Y. Wang, G.M. Jiang, Y.T. Chen, X.H. Xu, R.H. Hurt, Aerosol synthesis of phase-controlled iron-graphene nanohybrids through FeOOH nanorod intermediates, Environ. Sci: Nano, 3 (2016) 1215–1221.
[33] J. Huang, Q. Chang, Y. Ding, X. Han, H. Tang, Catalytic oxidative removal of 2,4-dichlorophenol by simultaneous use of horseradish peroxidase and graphene oxide/Fe_3O_4 as catalyst, Chem. Eng. J., 254 (2014) 434–442.
[34] Q. Chang, J. Huang, Y. Ding, H. Tang, Catalytic oxidation of phenol and 2,4-dichlorophenol by using horseradish peroxidase immobilized on graphene oxide/Fe_3O_4, Molecules, 21 (2016) 1044–1050.
[35] J. Cao, Q. Liu, J. Du, L. Yang, M. Wei, M. Gao, J. Yang, Facile one-step hydrothermal method to fabricate Fe_3O_4 quantum dots–graphene nanocomposites for extraction of dye from aqueous solution, J. Mater. Sci. Mater. Electron., 28 (2016) 2267–2271.
[36] J.W. Su, Y.X. Zhang, S.C. Xu, S. Wang, H.L. Ding, S.S. Pan, G.Z. Wang, G.H. Li, H.J. Zhao, Highly efficient and recyclable triple-shelled Ag@Fe_3O_4@SiO_2@TiO_2 photocatalysts for degradation of organic pollutants and reduction of hexavalent chromium ions, Nanoscale, 6 (2014) 5181–5192.
[37] H. Xu, Synthesis and super capacitance of goethite/reduced graphene oxide for supercapacitors, Mater. Chem. Phys., 141 (2013) 310–317.
[38] Q. Zhou, Y. Lin, J. Shu, K. Zhang, Z. Yu, D. Tang, Reduced graphene oxide-functionalized FeOOH for signal-on photoelectrochemical sensing of prostate-specific antigen with bioresponsive controlled release system, Biosens. Bioelectron., 98 (2017) 15–21.
[39] G. Huang, C. Zhang, Y. Long, J. Wynn, Y. Liu, W. Wang, J. Gao, Low temperature preparation of α-FeOOH/reduced graphene oxide and its catalytic activity for the photodegradation of an organic dye, Nanotechnology, 24 (2013) 395601–395601.
[40] P. Laokul, V. Amornkitbamrung, S. Seraphin, S. Maensiri, Characterization and magnetic properties of nanocrystalline CuFeO, NiFeO, ZnFeO powders prepared by the Aloe vera extract solution, Curr. Appl. Phys., 11 (2011) 101–108.
[41] F. Deng, X. Lu, X. Pei, X. Luo, S. Luo, D.D. Dionysiou, Fabrication of ternary reduced graphene oxide/SnS_2/$ZnFe_2O_4$ composite for high visible-light photocatalytic activity and stability, J. Hazard. Mater., 332 (2017) 149–161.
[42] B. Zhang, J. Zhang, F. Chen, Preparation and characterization of magnetic TiO_2/$ZnFe_2O_4$ photocatalysts by a sol–gel method, Res. Chem. Intermed., 34 (2008) 375–380.
[43] S. Sindhu, A. Narayanasamy, On the magnetic properties of ultra-fine zinc ferrites, J. Magn. Magn. Mater., 189 (1998) 83–88.
[44] B.K. Kang, Efficient removal of arsenic by strategically designed and layer-by-layer assembled PS@+rGO@GO@Fe_3O_4 composites, J. Environ. Manage., 201 (2017) 286–293.
[45] Z.J. Li, L. Wang, L.Y. Yuan, C.L. Xiao, L. Mei, L.R. Zheng, J. Zhang, J.H. Yang, Y.L. Zhao, Z.T. Zhu, Z.F. Chai, W.Q. Shi, Efficient removal of uranium from aqueous solution by zero-valent iron nanoparticle and its graphene composite, J. Hazard. Mater., 290 (2015) 26–33.
[46] W. Feng, P. Long, Y. Feng, Y. Li, Two-dimensional fluorinated graphene: synthesis, structures, properties and applications, Adv. Sci., 3 (2016) 1–22.
[47] H. Zhang, X. Lv, Y. Li, Y. Wang, J. Li, P25-graphene composite as a high performance photocatalyst, ACS Nano, 4 (2010) 380–386.
[48] S.V. Morozov, K.S. Novoselov, M.I. Katsnelson, F. Schedin, L.A. Ponomarenko, D. Jiang, A.K. Geim, Strong suppression of weak localization in graphene, Phys. Rev. Lett., 97 (2006) 016801–016804.
[49] E.H. Hwang, S. Adam, S.D. Sarma, Transport in chemically doped graphene in the presence of adsorbed molecules, Phys. Rev. B, 76 (2007) 195421–195429.
[50] M. Ishigami, J.H. Chen, W.G. Cullen, M.S. Fuhrer, E.D. Williams, Atomic Structure of Graphene on SiO_2, Nano Lett., 7 (2007) 1643–1648.
[51] F. Schedin, K.S. Novoselov, S.V. Morozov, D. Jiang, E.H. Hill, P. Blake, A.K. Geim, Detection of individual gas molecules by graphene sensors, Nat. Mater., 6 (2006) 652–655.
[52] T.O. Wehling, A.V. Balatsky, M.I. Katsnelson, A.I. Lichtenstein, K. Scharnberg, R. Wiesendanger, Local electronic signatures of impurity states in graphene, Phys. Rev. B, 75 (2007) 125421–125425.
[53] Y. Niimi, T. Matsui, H. Kambara, K. Tagami, M. Tsukada, H. Fukuyama, Scanning tunneling microscopy and spectroscopy of the electronic local density of states of graphite surfaces near monoatomic step edges, Phys. Rev. B, 73 (2006) 085421–0854218.
[54] M. Liang, B. Luo, L. Zhi, Application of graphene and graphene-based materials in clean energy-related devices, Int. J. Energy Res., 33 (2010) 1161–1170.
[55] S. Wang, H. Sun, H.M. Ang, M.O. Tadé, Adsorptive remediation of environmental pollutants using novel graphene-based nanomaterials, Chem. Eng. J., 226 (2013) 336–347.
[56] O.C. Compton, S.B.T. Nguyen, Graphene oxide, highly reduced graphene oxide, and graphene: versatile building blocks for carbon-based materials, Small, 6 (2010) 711–720.
[57] A. Kumar, L. Rout, L.S.K. Achary, S.K. Mohanty, P. Dash, A combustion synthesis route for magnetically separable graphene oxide–$CuFe_2O_4$–ZnO nanocomposites with enhanced solar light-mediated photocatalytic activity, New J. Chem., 41 (2017) 2–19.
[58] L. Zhuo, Y. Wu, L. Wang, J. Ming, Y. Yu, X. Zhang, F. Zhao, CO_2–expanded ethanol chemical synthesis of a Fe_3O_4@graphene composite and its good electrochemical properties as anode material for Li-ion batteries, J. Mater. Chem., 1 (2013) 3954–3960.
[59] S. Hashemian, M. Rahimi, A.A. Kerdegari, CuFeO@graphene nanocomposite as a sorbent for removal of alizarine yellow azo dye from aqueous solutions, Desal. Wat. Treat., 57 (2015) 1–12.
[60] J. Manokaran, Equilibrium, kinetic and thermodynamic studies for the removal of Zn(II) and Ni(II) ions using magnetically recoverable graphene/FeO composite, Desal. Wat. Treat., 56 (2015) 2485–2501.
[61] S. Vadahanambi, S.H. Lee, W.J. Kim, I.K. Oh, Arsenic removal from contaminated water using three-dimensional graphene-carbon nanotube-iron oxide nanostructures, Environ. Sci. Technol., 47 (2013) 10510–10517.
[62] C.M. Babu, R. Vinodh, B. Sundaravel, A. Abidov, M.P. Mei, S.C. Wang, H.T. Jang, Characterization of reduced graphene oxide supported mesoporous Fe_2O_3/TiO_2 nanoparticles and adsorption of As(III) and As(V) from potable water, J. Taiwan Inst. Chem. Eng., 62 (2016) 199–208.
[63] D.R. Dreyer, S. Park, C.W. Bielawski, R.S. Ruoff, The chemistry of graphene oxide, Chem. Soc. Rev., 39 (2009) 228–240.
[64] W. Gao, M. Majumder, L.B. Alemany, T.N. Narayanan, M.A. Ibarra, B.K. Pradhan, P.M. Ajayan, Engineered graphite oxide materials for application in water purification, ACS Appl. Mater. Interface, 3 (2011) 1821–1830.
[65] R. Mukherjee, P. Bhunia, S. De, Impact of graphene oxide on removal of heavy metals using mixed matrix membrane, Chem. Eng. J., 292 (2016) 284–297.
[66] Y. Bian, Z.Y. Bian, J.X. Zhang, A.Z. Ding, S.L. Liu, H. Wang, Effect of the oxygen-containing functional group of graphene oxide on the aqueous cadmium ions removal, Appl. Surf. Sci., 329 (2015) 269–275.
[67] B. Huang, Effect of Cu(II) ions on the enhancement of tetracycline adsorption by Fe_3O_4@SiO_2-Chitosan/Graphene oxide nanocomposite, Carbohydr. Polym., 157 (2017) 576–585.
[68] S. Yang, C. Chen, Y. Chen, J. Li, D. Wang, X. Wang, W. Hu, Competitive adsorption of Pb(II), Ni(II), and Sr(II) ions on graphene oxides: a combined experimental and theoretical study, Chempluschem, 80 (2015) 480–484.
[69] J. Xu, L. Wang, Y. Zhu, Decontamination of bisphenol a from aqueous solution by graphene adsorption, Langmuir, 28 (2012) 8418–8423.
[70] M. Machida, T. Mochimaru, H. Tatsumoto, Lead(II) adsorption onto the graphene layer of carbonaceous materials in aqueous solution, Carbon, 44 (2006) 2681–2688.
[71] Q. Chang, G. Jiang, H. Tang, N. Li, J. Huang, L. Wu, Enzymatic removal of chlorophenols using horseradish peroxidase

immobilized on superparamagnetic Fe_3O_4/graphene oxide nanocomposite, Chin. J. Catal., 36 (2015) 961–968.
[72] G. Jiang, TiO_2 nanoparticles assembled on graphene oxide nanosheets with high photocatalytic activity for removal of pollutants, Carbon, 49 (2011) 2693–2701.
[73] X. Yang, C. Chen, J. Li, G. Zhao, X. Ren, X. Wang, Graphene oxide-iron oxide and reduced graphene oxide-iron oxide hybrid materials for the removal of organic and inorganic pollutants, RSC Adv., 2 (2012) 8821–8826.
[74] S. Prakash, S. Mishra, Graphene-Fe_3O_4-TiO_2 ternary composite: an efficient visible light catalyst for the removal of organic pollutants, Neuropsychologia, 64 (2014) 124–133.
[75] L.M. Viculis, J.J. Mack, O.M. Mayer, H.T. Hahn, R. Kaner, Intercalation and exfoliation routes to graphite nanoplatelets, J. Mater. Chem., 15 (2005) 974–978.
[76] W. Choi, I. Lahiri, R. Seelaboyina, Y.S. Kang, Synthesis of graphene and its applications: a review, Crit. Rev. Solid State Mater. Sci., 35 (2010) 52–71.
[77] L.M. Viculis, J.J. Mack, R.B. Kaner, A chemical route to carbon nanoscrolls, Science, 299 (2003) 1361–1369.
[78] P.R. Somani, S.P. Somani, M. Umeno, Planer nano-graphenes from camphor by CVD, Chem. Phys. Lett., 430 (2006) 56–59.
[79] A.N. Obraztsov, E.A. Obraztsova, A.V. Tyurnina, A.A. Zolotukhin, Chemical vapor deposition of thin graphite films of nanometer thickness, Carbon, 45 (2007) 2017–2021.
[80] W. Zhao, M. Fang, F. Wu, H. Wu, L. Wang, G. Chen, Preparation of graphene by exfoliation of graphite using wet ball milling, J. Mater. Chem., 20 (2010) 5817–5819.
[81] P.T.L. Huong, T.H. Le, V.N. Phan, T.Q. Huy, H.N. Man, V.D. Lam, A.T. Le, Application of graphene oxide-$MnFe_2O_4$ magnetic nanohybrids as magnetically separable adsorbent for highly efficient removal of arsenic from water, J. Electron. Mater., 45 (2016) 2372–2380.
[82] C. Prasad, P.K. Murthy, R.H. Krishna, R.S. Rao, V. Suneetha, P. Venkateswarlu, Bio-inspired green synthesis of RGO/Fe_3O_4 magnetic nanoparticles using Murrayakoenigii leaves extract and its application for removal of Pb(II) from aqueous solution, J. Environ. Chem. Eng., 5 (2017) 1–31.
[83] Z. Wan, J. Wang, Degradation of sulfamethazine using Fe_3O_4-Mn_3O_4/reduced graphene oxide hybrid as Fenton-like catalyst, J. Hazard. Mater., 324 (2016) 653–664.
[84] A.K. Rai, S. Kim, J. Gim, M.H. Alfaruqi, V. Mathew, J. Kim, Electrochemical lithium storage of a $ZnFe_2O_4$/graphene nanocomposite as an anode material for rechargeable lithium ion batteries, RSC Adv., 4 (2014) 47087–47095.
[85] J. Zhu, M. Xu, X. Meng, K. Shang, H. Fan, S. Ai, Electroenzymatic degradation of carbofuran with the graphene oxide–Fe_3O_4–hemoglobin composite in an electrochemical reactor, Process Biochem., 47 (2012) 2480–2486.
[86] Y. Guo, Enhanced photocatalytic reduction activity of uranium(VI) from aqueous solution using the Fe_2O_3-graphene oxide nanocomposite, Dalton Trans., 2 (2017) 1–3.
[87] S. Chella, Solvothermal synthesis of $MnFe_2O_4$-graphene composite—investigation of its adsorption and antimicrobial properties, Appl. Surf. Sci., 327 (2015) 27–36.
[88] Y. Lin, Ternary Graphene–TiO_2–Fe_3O_4 Nanocomposite as a Recollectable Photocatalyst with Enhanced Durability, Eur. J. Inorg. Chem., 28 (2012) 4439–4444.
[89] D. Zhao, X. Gao, C. Wu, R. Xie, S. Feng, C. Chen, Facile preparation of amino functionalized graphene oxide decorated with Fe_3O_4 nanoparticles for the adsorption of Cr(VI), Appl. Surf. Sci., 384 (2016) 1–9.
[90] Y. Fu, X. Wang, Magnetically separable $ZnFe_2O_4$–graphene catalyst and its high photocatalytic performance under visible light irradiation, Ind. Eng. Chem. Res., 50 (2011) 7210–7218.
[91] X.L. Wu, Y. Shi, S. Zhong, H. Lin, J.R. Chen, Facile synthesis of Fe_3O_4-graphene@mesoporous SiO_2 nanocomposites for efficient removal of methylene blue, Appl. Surf. Sci., 378 (2016) 80–86.
[92] X.L. Wu, L. Wang, C.L. Chen, A.W. Xu, X.K. Wang, Water-dispersible magnetite-graphene-LDH composites for efficient arsenate removal, J. Mater. Chem., 21 (2011) 17353–17359.
[93] L. Li, J. Hu, X. Shi, M. Fan, J. Luo, X. Wei, Nanoscale zero-valent metals: a review of synthesis, characterization, and applications to environmental remediation, Environ. Sci. Pollut. Res., 23 (2016) 17880–17885.
[94] M.P. Deosarkar, S.M. Pawar, S.H. Sonawane, B.A. Bhanvase, Process intensification of uniform loading of SnO_2 nanoparticles on graphene oxide nanosheets using a novel ultrasound assisted in situ chemical precipitation method, Chem. Eng. Processing:Process Intensif., 70 (2013) 48–54.
[95] M.P. Deosarkar, S.M. Pawar, B.A. Bhanvase, In situ sonochemical synthesis of Fe_3O_4–graphene nanocomposite for lithium rechargeable batteries, Chem. Eng. Processing: Process Intensif., 83 (2014) 49–55.
[96] N. Rahman, U. Haseen, Equilibrium modeling, kinetic, and thermodynamic studies on adsorption of Pb(II) by a hybrid inorganic–organic material: polyacrylamide zirconium(IV), iodate. Ind. Eng. Chem. Res., 53 (2014) 8198–8207.
[97] S. Chandra, S. Bag, R. Bhar, P. Pramanik, Sonochemical synthesis and application of rhodium–graphene nanocomposite, J. Nanopart. Res., 13 (2010) 2769–2777.
[98] X.F. Zhang, L.L. Du, H. Wang, X.L. Dong, X.X. Zhang, C.C. Ma, H.C. Ma, Highly ordered mesoporous $BiVO_4$: controllable ordering degree and super photocatalytic ability under visible light, Microporous Mesoporous Mater., 173 (2013) 175–180.
[99] D. Zhao, EDTA functionalized Fe_3O_4/graphene oxide for efficient removal of U(VI) from aqueous solutions, J. Colloid Interface Sci., 506 (2017) 300–308.
[100] G.W. Zhou, Facile spray drying route for the three-dimensional graphene-encapsulated Fe_2O_3 nanoparticles for lithium ion battery anodes, Ind. Eng. Chem. Res., 52 (2013) 1197–1204.
[101] X. Huang, Y. Niu, W. Hu, Fe/Fe_3C nanoparticles loaded on Fe/N-doped graphene as an efficient heterogeneous fenton catalyst for degradation of organic pollutants, Colloids Surf., A, 518 (2017) 145–150.
[102] C. Lamberti, The use of synchrotron radiation techniques in the characterization of strained semiconductor heterostructures and thin films, Surf. Sci. Rep., 53 (2004) 186–197.
[103] S.D. Taylor, J. Liu, B.W. Arey, D.K. Schreiber, D.E. Perea, K.M. Rosso, Resolving Fe(II) sorption and oxidative growth on hematite (001) using atom probe tomography, J. Phys. Chem. C, 122 (2018) 3903–3914.
[104] S.D. Taylor, M.C. Marcano, U. Becker, A first principles investigation of electron transfer between Fe(II) and U(VI) on insulating Al- vs. semiconducting Fe-oxide surfaces via the proximity effect, Geochim. Cosmochim. Acta, 197 (2016) 1–38.
[105] S.E. Franklin, R.A. Stark, Application of secondary ion mass spectrometry to study of graphite morphology in cast iron, Metal Sci., 18 (1984) 187–199.
[106] F. Beate, V. Andreas, K. Ruben, Redox-controlled changes in cadmium solubility and solid-phase speciation in a paddy soil as affected by reducible sulfate and copper, Environ. Sci. Technol., 47 (2013) 12775–12783.
[107] M. Fan, T. Li, J. Hu, R. Cao, Q. Wu, X. Wei, L. Li, X. Shi, W. Ruan, Synthesis and characterization of reduced graphene oxide-supported nanoscale zero-valent iron (nZVI/rGO) composites used for Pb(II) removal, Materials, 9 (2016) 687–692.
[108] A. Boyde, E. Maconnachie, S.A. Reid, G. Delling, G.R. Mundy, Scanning electron microscopy in bone pathology: review of methods, potential and applications, Scan Electron Microsc., 6 (1986) 1537–1554.
[109] P. Echlin, Low temperature scanning electron microscopy: a review, J. Microsc., 112 (2011) 47–61.
[110] W.Q. Ruan, J.W. Hu, J.M. Qi, Y. Hou, R.S. Cao, X.H. Wei, Removal of crystal violet by using reduced-graphene-oxide-supported bimetallic Fe/Ni nanoparticles (rGO/Fe/Ni): application of artificial intelligence modeling for the optimization process, Materials, 11 (2018) 865–871.
[111] T. Shojaeimehr, F. Rahimpour, M.A. Khadivi, M. Sadeghi, A modeling study by response surface methodology (RSM) and artificial neural network (ANN) on Cu^{2+} adsorption optimization using light expended clay aggregate (LECA), J. Ind. Eng. Chem., 20 (2014) 870–880.

[112] Z. Gao, D. Zhang, Y. Ge, Design optimization of a spatial six degree-of-freedom parallel manipulator based on artificial intelligence approaches, Robot. Cim. Int. Manuf., 26 (2010) 180–189.
[113] R. Cao, M. Fan, J. Hu, W. Ruan, X. Wu, X. Wei, Artificial intelligence based optimization for the Se(IV) removal from aqueous solution by reduced graphene oxide-supported nanoscale zero-valent iron composites, Materials, 11 (2018) 428–435.
[114] E.S. Elmolla, M. Chaudhuri, M.M. Eltoukhy, The use of artificial neural network (ANN) for modeling of COD removal from antibiotic aqueous solution by the Fenton process, J. Hazard. Mater., 179 (2010) 127–134.
[115] F. Heydari, M. Ghaedi, A. Ansari, A.M. Ghaedi, Random forest model for removal of methylene blue and lead(II) ion using activated carbon obtained from Tamarisk, Desal. Wat. Treat., 57 (2015) 1–19.
[116] S. Eslamian, N. Lavaei, Modelling nitrate pollution of groundwater using artificial neural network and genetic algorithm in an arid zone, Int. J. Water, 5 (2009) 194–203.
[117] P. Kundu, A. Debsarkar, S. Mukherjee, Artificial neural network modeling for biological removal of organic carbon and nitrogen from slaughterhouse wastewater in a sequencing Batch reactor, Adv. Artif. Neural Syst., 2013 (2013) 1–15.
[118] F.M. Santin, R.V.D. Silva, J.M.V. Grzybowski, Artificial neural network ensembles and the design of performance-oriented riparian buffer strips for the filtering of nitrogen in agricultural catchments, Ecol. Eng., 94 (2016) 493–502.
[119] M. Huang, J. Wan, Y. Ma, Monitoring of anoxic/oxic process for nitrogen and chemical oxygen demand removal using fuzzy neural networks, Water Environ. Res., 81 (2009) 654–663.
[120] Y. Zhang, B. Pan, Modeling batch and column phosphate removal by hydrated ferric oxide-based nanocomposite using response surface methodology and artificial neural network, Chem. Eng. J., 249 (2014) 111–120.
[121] S. Mandal, S.S. Mahapatra, M.K. Sahu, R.K. Patel, Artificial neural network modeling of As(III) removal from water by novel hybrid material, Process Saf. Environ., 93 (2015) 249–264.
[122] E.A. Dil, M. Ghaedi, A. Asfaram, S. Hajati, F. Mehrabi, A. Goudarzi, Preparation of nanomaterials for the ultrasound-enhanced removal of Pb^{2+} ions and malachite green dye: Chemometric optimization and modeling, Ultrason. Sonochem., 34 (2017) 677–691.
[123] T. Singh, V. Singh, S. Sinha, Prediction of cadmium removal using an artificial neural network and a neuro-fuzzy technique, Mine Water Environ., 25 (2006) 214–219.
[124] B.H. Lee, M. Scholz, Application of the self-organizing map (SOM) to assess the heavy metal removal performance in experimental constructed wetlands, Water Res., 40 (2006) 3367–3374.
[125] S. Chattoraj, N.K. Mondal, B. Das, P. Roy, B. Sadhukhan, Carbaryl removal from aqueous solution by Lemna major biomass using response surface methodology and artificial neural network, J. Environ. Chem. Eng., 2 (2014) 1920–1928.
[126] M. Wang, S. Wang, An optical performance monitoring model based on RBFANN trained with Eye-Diagram, Procedia Eng., 29 (2012) 53–57.
[127] A.A. Ismaiel, M.K. Aroua, R. Yusoff, Palm shell activated carbon impregnated with task-specific ionic-liquids as a novel adsorbent for the removal of mercury from contaminated water, Chem. Eng. J., 225 (2013) 306–314.
[128] H. Zheng, D.H. Liu, Y. Zheng, S.P. Liang, Z. Liu, Sorption isotherm and kinetic modeling of aniline on Cr-bentonite, J. Hazard. Mater., 167 (2009) 141–147.
[129] K.V. Kumar, K. Porkodi, F. Rocha, Comparison of various error functions in predicting the optimum isotherm by linear and non-linear regression analysis for the sorption of basic red 9 by activated carbon, J. Hazard. Mater., 150 (2008) 158–165.
[130] Y.S. Ho, Selection of optimum sorption isotherm, Carbon, 42 (2004) 2115–2116.
[131] A. Kausar, H.N. Bhatti, G. Mackinnon, Equilibrium, kinetic and thermodynamic studies on the removal of U(VI) by low cost agricultural waste, Colloids Surf., B, 111 (2013) 124–133.
[132] X. Rong, F. Qiu, J. Qin, H. Zhao, J. Yan, D. Yang, A facile hydrothermal synthesis, adsorption kinetics and isotherms to Congo Red azo-dye from aqueous solution of NiO/graphene nanosheets adsorbent, J. Ind. Eng. Chem., 26 (2015) 354–363.
[133] M. Alkan, Adsorption kinetics and thermodynamics of an anionic dye onto sepiolite, Mesoporous Mater., 101 (2007) 388–396.
[134] T. Qi, C. Huang, S. Yan, X.J. Li, S.Y. Pan, Synthesis, characterization and adsorption properties of magnetite/reduced graphene oxide nanocomposites, Talanta, 144 (2015) 1116–1124.
[135] E.A. Dil, Application of artificial neural network and response surface methodology for the removal of crystal violet by zinc oxide nanorods loaded on activate carbon: kinetics and equilibrium study, J. Taiwan Inst. Chem. Eng., 59 (2016) 210–220.
[136] V. Srivastava, Y.C. Sharma, M. Sillanpää, Application of nano-magnesso ferrite (n-$MgFe_2O_4$) for the removal of Co^{2+} ions from synthetic wastewater: kinetic, equilibrium and thermodynamic studies, Appl. Surf. Sci., 338 (2015) 42–54.
[137] A. Çelekli, H. Bozkurt, F. Geyik, Artificial neural network and genetic algorithms for modeling of removal of an azo dye on walnut husk, Desal. Wat. Treat., 57 (2015) 1–12.
[138] M.I. Inyang, A review of biochar as a low-cost adsorbent for aqueous heavy metal removal, Crit. Rev. Environ. Sci. Technol., 46 (2016) 1–56.
[139] Z. Liu, F.S. Zhang, Removal of lead from water using biochars prepared from hydrothermal liquefaction of biomass, J. Hazard. Mater., 167 (2009) 933–939.
[140] W.K. Park, Feasible water flow filter with facilely functionalized Fe_3O_4-non-oxidative graphene/CNT composites for arsenic removal, J. Environ. Chem. Eng., 4 (2016) 3246–3252.
[141] P.K. Boruah, B. Sharma, N. Hussain, M.R. Das, Magnetically recoverable Fe_3O_4/graphene nanocomposite towards efficient removal of triazine pesticides from aqueous solution: investigation of the adsorption phenomenon and specific ion effect, Chemosphere, 168 (2017) 1058–1062.
[142] M. Fan, T. Li, J. Hu, R. Cao, X. Wei, X. Shi, W. Ruan, Artificial neural network modeling and genetic algorithm optimization for cadmium removal from aqueous solutions by reduced graphene oxide-supported nanoscale zero-valent iron (nZVI/rGO) composites, Materials, 10 (2017) 544–551.
[143] W. Fan, W. Gao, C. Zhang, W.T. Weng, J. Pan, T. Liu, Hybridization of graphene sheets and carbon-coated Fe_3O_4 nanoparticles as a synergistic adsorbent of organic dyes, J. Mater. Chem., 22 (2012) 25108–25115.
[144] S. Kumar, R.R. Nair, P.B. Pillai, S.N. Gupta, M.A.R. Iyengar, A.K. Sood, Graphene oxide-$MnFe_2O_4$ magnetic nanohybrids for efficient removal of lead and arsenic from water, ACS Appl. Mater. Interface, 6 (2014) 17426–17430.
[145] X. Shi, W. Ruan, J. Hu, M. Fan, R. Cao, X. Wei, Optimizing the removal of rhodamine B in aqueous solutions by reduced graphene oxide-supported nanoscale zerovalent iron (nZVI/rGO) using an artificial neural network-genetic algorithm (ANN-GA), Nanomaterials, 7 (2017) 309–315.
[146] L. Chen, S. Feng, D. Zhao, S. Chen, F. Li, C. Chen, Efficient sorption and reduction of U(VI) on zero-valent iron-polyaniline-graphene aerogel ternary composite, J. Colloid Interface Sci., 490 (2017) 197–203.
[147] L.Y. Zhu, X.Y. Zeng, X.P. Li, P. Yang, R.H. Yun, Hydrothermal synthesis of magnetic Fe_3O_4/graphene composites with good electromagnetic microwave absorbing performances, J. Magn. Magn. Mater., 426 (2017) 114–120.
[148] S. Nethaji, A. Sivasamy, Graphene oxide coated with porous iron oxide ribbons for 2, 4-Dichlorophenoxyacetic acid (2,4-D) removal, Ecotoxicol, Environ. Saf., 138 (2017) 292–297.
[149] H.V. Tran, L.T. Bui, T.T. Dinh, D.H. Le, C.D. Huynh, A.X. Trinh, Graphene oxide/Fe_3O_4/chitosan nanocomposite: a recoverable and recyclable adsorbent for organic dyes

removal. Application to methylene blue, Mater. Res. Express., 4 (2017) 701–711.
[150] A. Sinha, N.R. Jana, Graphene-based composite with γ-Fe_2O_3 nanoparticle for the high-performance removal of endocrine-disrupting compounds from water, Chem. Asian J., 8 (2013) 786–791.
[151] X.L. Wu, P. Xiao, S. Zhong, K. Fang, H. Lin, J. Chen, Magnetic $ZnFe_2O_4$@chitosan encapsulated in graphene oxide for adsorptive removal of organic dye, RSC Adv., 7 (2017) 28145–28151.
[152] N.U. Yamaguchi, R. Bergamasco, S. Hamoudi, Magnetic $MnFe_2O_4$–graphene hybrid composite for efficient removal of glyphosate from water, Chem. Eng. J., 295 (2016) 391–402.
[153] Y.J. Yao, Magnetic recoverable $MnFe_2O_4$ and $MnFe_2O_4$-graphene hybrid as heterogeneous catalysts of peroxymonosulfate activation for efficient degradation of aqueous organic pollutants, J. Hazard. Mater., 270 (2014) 61–70.
[154] A. Muthukrishnaraj, J. Manokaran, M. Vanitha, K.V. Thiruvengadaravi, P. Baskaralingam, N. Balasubramanian, Equilibrium, kinetic and thermodynamic studies for the removal of Zn(II) and Ni(II) ions using magnetically recoverable graphene/Fe_3O_4 composite, Desal. Wat. Treat., 56 (2015) 2485–2501.
[155] T.Q. Dat, N.T. Ha, D.Q. Hung, Reduced graphene oxide-$Cu_{0.5}Ni_{0.5}Fe_2O_4$-polyaniline nanocomposite: preparation, characterization and microwave absorption properties, J. Electron. Mater., 46 (2017) 3707–3713.
[156] J. Liu, W. Liu, Y. Wang, M. Xu, B. Wang, A novel reusable nanocomposite adsorbent, xanthated Fe_3O_4-chitosan grafted onto graphene oxide, for removing Cu(II) from aqueous solutions, Appl. Surf. Sci., 367 (2016) 327–334.
[157] H. Jabeen, V. Chandra, S. Jung, Enhanced Cr(VI) removal using iron nanoparticle decorated graphene, Nanoscale, 3 (2011) 3583–3585.
[158] M. Fan, J. Hu, R. Cao, K. Xiong, X. Wei, Modeling and prediction of copper removal from aqueous solutions by nZVI/rGO magnetic nanocomposites using ANN-GA and ANN-PSO, Sci. Rep., 7 (2017) 1–14.
[159] C.M. Babu, B. Palanisamy, B. Sundaravel, K. Shanthi, V. Murugesan, Dihalogen crosslinked Fe_3O_4-reduced graphene oxide nanocomposites for arsenic and mercury adsorption, Sci. Adv. Mater., 7 (2015) 794–805.
[160] J. Barker, Enhanced adsorption of carbon nanocomposites exhausted with 2,4-dichlorophenoxyacetic acid after regeneration by thermal oxidation and microwave irradiation, Environ. Sci. Nano, 1 (2014) 113–116.
[161] R. Cao, M. Fan, J. Hu, W. Ruan, K. Xiong, X. Wei, Optimizing low-concentration mercury removal from aqueous solutions by reduced graphene oxide-supported Fe_3O_4 composites with the aid of an artificial neural network and genetic algorithm, Materials, 10 (2017) 1–17.
[162] Z. Clemente, V.L. Castro, C.M. Jonsson, L.F. Fraceto, Ecotoxicology of nano-TiO_2 an evaluation of its toxicity to organisms of aquatic ecosystems, Int. J. Environ. Res., 6 (2011) 33–50.
[163] L. Li, J. Hu, X. Shi, M. Fan, L. Jin, X. Wei, Nanoscale zero-valent metals: a review of synthesis, characterization, and applications to environmental remediation, Environ. Sci. Pollut. Res., 23 (2016) 1–21.
[164] R.D. Handy, R. Owen, E. Valsami-Jones, The ecotoxicology of nanoparticles and nanomaterials: current status, knowledge gaps, challenges, and future needs, Ecotoxicology, 17 (2008) 315–325.
[165] M. Markovic, Ecotoxicology of manufactured graphene oxid nanomaterials and derivation of preliminary guideline values for freshwater environments, Environ. Toxicol. Chem., 37 (2018) 1340–1348.
[166] M.I.N. Ahamed, Ecotoxicity concert of nano zero-valent iron particles-a review, J. Crit. Rev., 6 (2014) 112–120.
[167] Y.S. Temsah, E.J. Joner, Ecotoxicological effects on earthworms of fresh and aged nano-sized zero-valent iron (nZVI) in soil, Chemosphere, 89 (2012) 76–82.
[168] D. Rede, Lúcia H.M.L.M. Santos, S. Ramos, F. Oliva-Teles, C. Antao, S.R. Sousa, C. Delerue-Matos, Ecotoxicological impact of two soil remediation treatments in lactuca sativa seeds, Chemosphere, 159 (2016) 193–198.
[169] X. Lv, Removal of chromium(VI) from wastewater by nanoscale zero-valent iron particles supported on multiwalled carbon nanotubes, Chemosphere, 85 (2011) 1204–1209.
[170] T. Zheng, Reactivity characteristics of nanoscale zerovalent iron--silica composites for trichloroethylene remediation, Environ. Sci. Technol., 42 (2008) 4494–4499.
[171] A. Tamion, E. Cadel, C. Bordel, D. Blavette, 3D atom probe investigation of (Fe/Dy) magnetic multilayers, Surf. Interface Anal., 39 (2007) 237–239.